

An Enigmatic PeVatron in an Area around HII Region G35.6–0.5

ZHEN CAO,^{1,2,3} F. AHARONIAN,^{4,5} AXIKEGU,⁶ Y.X. BAI,^{1,3} Y.W. BAO,⁷ D. BASTIERI,⁸ X.J. BI,^{1,2,3} Y.J. BI,^{1,3} W. BIAN,⁹
A.V. BUKEVICH,¹⁰ Q. CAO,¹¹ W.Y. CAO,¹² ZHE CAO,^{13,12} J. CHANG,¹⁴ J.F. CHANG,^{1,3,13} A.M. CHEN,⁹ B.Q. CHEN,¹⁵
E.S. CHEN,^{1,2,3} H.X. CHEN,¹⁶ LIANG CHEN,¹⁷ LIN CHEN,⁶ LONG CHEN,⁶ M.J. CHEN,^{1,3} M.L. CHEN,^{1,3,13} Q.H. CHEN,⁶
S. CHEN,¹⁸ S.H. CHEN,^{1,2,3} S.Z. CHEN,^{1,3} T.L. CHEN,¹⁹ Y. CHEN ⁷, N. CHENG,^{1,3} Y.D. CHENG,^{1,2,3} M.C. CHU,²⁰
M.Y. CUI,¹⁴ S.W. CUI,¹¹ X.H. CUI,²¹ Y.D. CUI,²² B.Z. DAI,¹⁸ H.L. DAI,^{1,3,13} Z.G. DAI,¹² DANZENGLUOBU,¹⁹
X.Q. DONG,^{1,2,3} K.K. DUAN,¹⁴ J.H. FAN,⁸ Y.Z. FAN,¹⁴ J. FANG,¹⁸ J.H. FANG,¹⁶ K. FANG,^{1,3} C.F. FENG,²³ H. FENG,¹
L. FENG,¹⁴ S.H. FENG,^{1,3} X.T. FENG,²³ Y. FENG,¹⁶ Y.L. FENG,¹⁹ S. GABICI,²⁴ B. GAO,^{1,3} C.D. GAO,²³ Q. GAO,¹⁹
W. GAO,^{1,3} W.K. GAO,^{1,2,3} M.M. GE,¹⁸ T.T. GE,²² L.S. GENG,^{1,3} G. GIACINTI,⁹ G.H. GONG,²⁵ Q.B. GOU,^{1,3}
M.H. GU,^{1,3,13} F.L. GUO,¹⁷ J. GUO,²⁵ X.L. GUO,⁶ Y.Q. GUO,^{1,3} Y.Y. GUO,¹⁴ Y.A. HAN,²⁶ O.A. HANNUKSELA,²⁰
M. HASAN,^{1,2,3} H.H. HE,^{1,2,3} H.N. HE,¹⁴ J.Y. HE,¹⁴ Y. HE,⁶ Y.K. HOR,²² B.W. HOU,^{1,2,3} C. HOU,^{1,3} X. HOU,²⁷
H.B. HU,^{1,2,3} Q. HU,^{12,14} S.C. HU,^{1,3,28} C. HUANG,⁷ D.H. HUANG,⁶ T.Q. HUANG,^{1,3} W.J. HUANG,²² X.T. HUANG,²³
X.Y. HUANG,¹⁴ Y. HUANG,^{1,2,3} Y.Y. HUANG,⁷ X.L. JI,^{1,3,13} H.Y. JIA,⁶ K. JIA,²³ H.B. JIANG,^{1,3} K. JIANG,^{13,12}
X.W. JIANG,^{1,3} Z.J. JIANG,¹⁸ M. JIN,⁶ M.M. KANG,²⁹ I. KARPIKOV,¹⁰ D. KHANGULYAN,^{1,3} D. KULESHOV,¹⁰ K. KURINOV,¹⁰
B.B. LI,¹¹ C.M. LI,⁷ CHENG LI,^{13,12} CONG LI,^{1,3} D. LI,^{1,2,3} F. LI,^{1,3,13} H.B. LI,^{1,3} H.C. LI,^{1,3} JIAN LI,¹² JIE LI,^{1,3,13}
K. LI,^{1,3} S.D. LI,^{17,2} W.L. LI,²³ W.L. LI,⁹ X.R. LI,^{1,3} XIN LI,^{13,12} Y.Z. LI,^{1,2,3} ZHE LI,^{1,3} ZHUO LI,³⁰ E.W. LIANG,³¹
Y.F. LIANG,³¹ S.J. LIN,²² B. LIU,¹² C. LIU,²³ D. LIU,²³ D.B. LIU,⁹ H. LIU,⁶ H.D. LIU,²⁶ J. LIU,^{1,3} J.L. LIU,^{1,3}
M.Y. LIU,¹⁹ R.Y. LIU,⁷ S.M. LIU,⁶ W. LIU,^{1,3} Y. LIU,⁸ Y.N. LIU,²⁵ Q. LUO,²² Y. LUO,⁹ H.K. LV,^{1,3} B.Q. MA,³⁰
L.L. MA,^{1,3} X.H. MA,^{1,3} J.R. MAO,²⁷ Z. MIN,^{1,3} W. MITTHUMSIRI,³² H.J. MU,²⁶ Y.C. NAN,^{1,3} A. NERONOV,²⁴
K.C.Y. NG,²⁰ L.J. OU,⁸ P. PATTARAKIJWANICH,³² Z.Y. PEI,⁸ J.C. QI,^{1,2,3} M.Y. QI,^{1,3} B.Q. QIAO,^{1,3} J.J. QIN,¹²
A. RAZA,^{1,2,3} D. RUFFOLO,³² A. SÁIZ,³² M. SAEED,^{1,2,3} D. SEMIKOZ,²⁴ L. SHAO,¹¹ O. SHCHEGOLEV,^{10,33} X.D. SHENG,^{1,3}
F.W. SHU,³⁴ H.C. SONG,³⁰ YU.V. STENKIN,^{10,33} V. STEPANOV,¹⁰ Y. SU,¹⁴ D.X. SUN,^{12,14} Q.N. SUN,⁶ X.N. SUN,³¹
Z.B. SUN,³⁵ J. TAKATA,³⁶ P.H.T. TAM,²² Q.W. TANG,³⁴ R. TANG,⁹ Z.B. TANG,^{13,12} W.W. TIAN,^{2,21} L.H. WAN,²²
C. WANG,³⁵ C.B. WANG,⁶ G.W. WANG,¹² H.G. WANG,⁸ H.H. WANG,²² J.C. WANG,²⁷ KAI WANG,⁷ KAI WANG,³⁶
L.P. WANG,^{1,2,3} L.Y. WANG,^{1,3} P.H. WANG,⁶ R. WANG,²³ W. WANG,²² X.G. WANG,³¹ X.Y. WANG,⁷ Y. WANG,⁶
Y.D. WANG,^{1,3} Y.J. WANG,^{1,3} Z.H. WANG,²⁹ Z.X. WANG,¹⁸ ZHEN WANG,⁹ ZHENG WANG,^{1,3,13} D.M. WEI,¹⁴ J.J. WEI,¹⁴
Y.J. WEI,^{1,2,3} T. WEN,¹⁸ C.Y. WU,^{1,3} H.R. WU,^{1,3} Q.W. WU,³⁶ S. WU,^{1,3} X.F. WU,¹⁴ Y.S. WU,¹² S.Q. XI,^{1,3}
J. XIA,^{12,14} G.M. XIANG,^{17,2} D.X. XIAO,¹¹ G. XIAO,^{1,3} Y.L. XIN,⁶ Y. XING,¹⁷ D.R. XIONG,²⁷ Z. XIONG,^{1,2,3} D.L. XU,⁹
R.F. XU,^{1,2,3} R.X. XU,³⁰ W.L. XU,²⁹ L. XUE,²³ D.H. YAN,¹⁸ J.Z. YAN,¹⁴ T. YAN,^{1,3} C.W. YANG,²⁹ C.Y. YANG,²⁷
F. YANG,¹¹ F.F. YANG,^{1,3,13} L.L. YANG,²² M.J. YANG,^{1,3} R.Z. YANG,¹² W.X. YANG,⁸ Y.H. YAO,^{1,3} Z.G. YAO,^{1,3}
L.Q. YIN,^{1,3} N. YIN,²³ X.H. YOU,^{1,3} Z.Y. YOU,^{1,3} Y.H. YU,¹² Q. YUAN,¹⁴ H. YUE,^{1,2,3} H.D. ZENG,¹⁴ T.X. ZENG,^{1,3,13}
W. ZENG,¹⁸ M. ZHA,^{1,3} B.B. ZHANG,⁷ F. ZHANG,⁶ H. ZHANG,⁹ H.M. ZHANG,⁷ H.Y. ZHANG,¹⁸ J.L. ZHANG,²¹ LI ZHANG,¹⁸
P.F. ZHANG,¹⁸ P.P. ZHANG,^{12,14} R. ZHANG,¹⁴ S.B. ZHANG,^{2,21} S.R. ZHANG,¹¹ S.S. ZHANG,^{1,3} X. ZHANG ^{37,7}
X.P. ZHANG,^{1,3} Y.F. ZHANG,⁶ YI ZHANG,^{1,14} YONG ZHANG,^{1,3} B. ZHAO,⁶ J. ZHAO,^{1,3} L. ZHAO,^{13,12} L.Z. ZHAO,¹¹
S.P. ZHAO,¹⁴ X.H. ZHAO,²⁷ F. ZHENG,³⁵ W.J. ZHONG ⁷, B. ZHOU,^{1,3} H. ZHOU,⁹ J.N. ZHOU,¹⁷ M. ZHOU,³⁴ P. ZHOU,⁷
R. ZHOU,²⁹ X.X. ZHOU,^{1,2,3} X.X. ZHOU,⁶ B.Y. ZHU,^{12,14} C.G. ZHU,²³ F.R. ZHU,⁶ H. ZHU,²¹ K.J. ZHU,^{1,2,3,13} Y.C. ZOU,³⁶
AND X. ZUO^{1,3}

¹Key Laboratory of Particle Astrophysics & Experimental Physics Division & Computing Center, Institute of High Energy Physics, Chinese Academy of Sciences, 100049 Beijing, China

²University of Chinese Academy of Sciences, 100049 Beijing, China

³TIANFU Cosmic Ray Research Center, Chengdu, Sichuan, China

⁴Dublin Institute for Advanced Studies, 31 Fitzwilliam Place, 2 Dublin, Ireland

⁵Max-Planck-Institut für Nuclear Physics, P.O. Box 103980, 69029 Heidelberg, Germany

⁶School of Physical Science and Technology & School of Information Science and Technology, Southwest Jiaotong University, 610031 Chengdu, Sichuan, China

⁷School of Astronomy and Space Science, Nanjing University, 210023 Nanjing, Jiangsu, China

⁸Center for Astrophysics, Guangzhou University, 510006 Guangzhou, Guangdong, China

⁹Tsung-Dao Lee Institute & School of Physics and Astronomy, Shanghai Jiao Tong University, 200240 Shanghai, China

¹⁰Institute for Nuclear Research of Russian Academy of Sciences, 117312 Moscow, Russia

¹¹Hebei Normal University, 050024 Shijiazhuang, Hebei, China

Corresponding author:

W.J. Zhong (wjzh@smail.nju.edu.cn),

X. Zhang (xiaozhang@nju.edu.cn),

Y. Chen (ygchen@nju.edu.cn)

¹²University of Science and Technology of China, 230026 Hefei, Anhui, China

¹³State Key Laboratory of Particle Detection and Electronics, China

¹⁴Key Laboratory of Dark Matter and Space Astronomy & Key Laboratory of Radio Astronomy, Purple Mountain Observatory, Chinese Academy of Sciences, 210023 Nanjing, Jiangsu, China

¹⁵South-Western Institute for Astronomy Research, Yunnan University, 650091 Kunming, Yunnan, China

¹⁶Research Center for Astronomical Computing, Zhejiang Laboratory, 311121 Hangzhou, Zhejiang, China

¹⁷Key Laboratory for Research in Galaxies and Cosmology, Shanghai Astronomical Observatory, Chinese Academy of Sciences, 200030 Shanghai, China

¹⁸School of Physics and Astronomy, Yunnan University, 650091 Kunming, Yunnan, China

¹⁹Key Laboratory of Cosmic Rays (Tibet University), Ministry of Education, 850000 Lhasa, Tibet, China

²⁰Department of Physics, The Chinese University of Hong Kong, Shatin, New Territories, Hong Kong, China

²¹Key Laboratory of Radio Astronomy and Technology, National Astronomical Observatories, Chinese Academy of Sciences, 100101 Beijing, China

²²School of Physics and Astronomy (Zhuhai) & School of Physics (Guangzhou) & Sino-French Institute of Nuclear Engineering and Technology (Zhuhai), Sun Yat-sen University, 519000 Zhuhai & 510275 Guangzhou, Guangdong, China

²³Institute of Frontier and Interdisciplinary Science, Shandong University, 266237 Qingdao, Shandong, China

²⁴APC, Université Paris Cité, CNRS/IN2P3, CEA/IRFU, Observatoire de Paris, 119 75205 Paris, France

²⁵Department of Engineering Physics & Department of Astronomy, Tsinghua University, 100084 Beijing, China

²⁶School of Physics and Microelectronics, Zhengzhou University, 450001 Zhengzhou, Henan, China

²⁷Yunnan Observatories, Chinese Academy of Sciences, 650216 Kunming, Yunnan, China

²⁸China Center of Advanced Science and Technology, Beijing 100190, China

²⁹College of Physics, Sichuan University, 610065 Chengdu, Sichuan, China

³⁰School of Physics, Peking University, 100871 Beijing, China

³¹Guangxi Key Laboratory for Relativistic Astrophysics, School of Physical Science and Technology, Guangxi University, 530004 Nanning, Guangxi, China

³²Department of Physics, Faculty of Science, Mahidol University, Bangkok 10400, Thailand

³³Moscow Institute of Physics and Technology, 141700 Moscow, Russia

³⁴Center for Relativistic Astrophysics and High Energy Physics, School of Physics and Materials Science & Institute of Space Science and Technology, Nanchang University, 330031 Nanchang, Jiangxi, China

³⁵National Space Science Center, Chinese Academy of Sciences, 100190 Beijing, China

³⁶School of Physics, Huazhong University of Science and Technology, Wuhan 430074, Hubei, China

³⁷School of Physics and Technology, Nanjing Normal University, 210023 Nanjing, Jiangsu, China

ABSTRACT

Identifying Galactic PeVatrons (PeV particle accelerators) from the ultra-high-energy (UHE, >100 TeV) γ -ray sources plays a crucial role in revealing the origin of Galactic cosmic rays. The UHE source 1LHAASO J1857+0203u is suggested to be associated with HESS J1858+020, which may be attributed to the possible PeVatron candidate supernova remnant (SNR) G35.6–0.4 or HII region G35.6–0.5. We perform detailed analysis on the very-high-energy and UHE γ -ray emissions towards this region with data from the Large High Altitude Air Shower Observatory (LHAASO). 1LHAASO J1857+0203u is detected with a significance of 11.6σ above 100 TeV, indicating the presence of a PeVatron. It has an extension of $\sim 0.18^\circ$ with a power-law (PL) spectral index of ~ 2.5 in 1–25 TeV and a point-like emission with a PL spectral index of ~ 3.2 above 25 TeV. Using the archival CO and HI data, we identify some molecular and atomic clouds that may be associated with the TeV γ -ray emissions. Our modelling indicates that the TeV γ -ray emissions are unlikely to arise from the clouds illuminated by the protons that escaped from SNR G35.6–0.4. In the scenario that HII region G35.6–0.5 could accelerate particles to the UHE band, the observed GeV–TeV γ -ray emission could be well explained by a hadronic model with a PL spectral index of ~ 2.0 and cutoff energy of ~ 450 TeV. However, an evolved pulsar wind nebula origin cannot be ruled out.

Keywords: Gamma-rays; Gamma-ray sources; HII regions; Supernova remnants

1. INTRODUCTION

The origin of cosmic rays (CRs) has remained elusive for more than one hundred years since their dis-

covery. According to γ -ray observations of the Galactic disk and the Magellanic clouds, it is suggested that the CRs below the so-called CR ‘knee’ ($\sim 3 \times 10^{15}$ eV) are produced in our Galaxy (e.g. Baade & Zwicky 1934; Ginzburg & Syrovatskii 1964). This indicates that particles can be accelerated up to peta-electron volt energies by some Galactic sources, called PeV particle accelerators or ‘PeVatrons’. The first strong evidence came from observations on the Galactic Centre by H.E.S.S. (HESS Collaboration et al. 2016), MAGIC (MAGIC Collaboration et al. 2020), and VERITAS (Adams et al. 2021), followed by more observations from HAWC on a few objects in the Galactic plane (Albert et al. 2020; Abeysekara et al. 2020, 2021). The discovery of dozens of sources by the Large High Altitude Air Shower Observatory (LHAASO) at ultra-high energy (UHE) above 100 TeV further confirms the existence of Galactic PeVatrons (Cao et al. 2021, 2024). Among the prominent PeVatron candidates, such as supernova remnants (SNRs), pulsars (PSRs) and their wind nebulae (PWNe), young massive star clusters or HII regions (HIIRs), etc (Chen et al. 2022), the dominance of PWNe has been established and explicitly reported by both LHAASO (e.g. Cao et al. 2021) and HAWC (e.g. Tibolla 2023). However, it is unknown which types of objects are hadronic PeVatrons. Studying the γ -rays produced by the CRs interacting with dense matter surrounding the acceleration site is an important and effective way to unveil the origin of Galactic CRs.

Radio complex G35.6–0.4 is likely associated with the unidentified extended TeV source HESS J1858+020 (Aharonian et al. 2008; H. E. S. S. Collaboration et al. 2018) and was suggested to be a hadronic PeVatron candidate (Zhang et al. 2022). With the Giant Metrewave Radio Telescope (GMRT) observations at 610 MHz (Paredes et al. 2014), the radio complex was resolved into two nearly circularly shaped extended sources, SNR G35.6–0.4 and HIIR G35.6–0.5. No diffuse X-ray emission but seven X-ray point sources (labelled as X1–7) were detected with a 29.8 ks *Chandra* observation in the region of HESS J1858+020 (Paredes et al. 2014). Among these sources, X1–4 might be embedded protostars projectively distributed on the shell of the HIIR, while X5 might be coincident with a star formation region and close to the southern molecular clump (see Paredes et al. 2014, Fig. 2). At GeV energies, the *Fermi* Large Area Telescope (LAT) Fourth Source Catalog Data Release 4 (4FGL-DR4, Abdollahi et al. 2022; Ballet et al. 2023) reported two point sources, 4FGL J1857.6+0212 and 4FGL J1858.3+0209, towards the G35.6–0.4 region. Of these two GeV sources, 4FGL J1858.3+0209 was re-localised as SrcX2 by Cui et al.

(2021) or SrcB by Zhang et al. (2022) and within the 7σ contour of HESS J1858+020. Considering an association with a $\sim +55$ km s $^{-1}$ molecular cloud (MC) complex (Paron & Giacani 2010), Cui et al. (2021) ascribed the GeV-TeV γ -ray emission to hadronic interaction between the molecular gas by the CR protons escaped from the SNR, which was suggested to be at a distance of ~ 3.6 kpc (Zhu et al. 2013). On the contrary, Zhang et al. (2022) argued that the SNR component G35.6–0.4 and the HIIR component G35.6–0.5 are mutually irrelevant objects at a far distance of ~ 10.5 kpc and a near distance of ~ 3.4 kpc, respectively, and the γ -rays are likely to arise from a high-energy source hidden in the HIIR. Additionally, the spatial associations and the well-connected GeV-TeV γ -ray spectrum which has no obvious cutoff seem to indicate a potential PeV proton accelerator in HIIR G35.6–0.5. As listed in the first LHAASO catalogue, an extended UHE γ -ray source, 1LHAASO J1857+0203u, was detected to be associated with HESS J1858+020 with a significance over 10σ above 100 TeV (Cao et al. 2024). Recently, HAWC Collaboration reported the preliminary update to their UHE catalogue, in which a point-like UHE γ -ray source, xHWC J1858+020, is also detected within the 6σ contour of HESS J1858+020 (Malone et al. 2023). However, they did not provide either the spectrum or flux points.

In this work, we present a detailed LHAASO observational data analysis towards the region of the SNR-HIIR complex G35.6–0.4. Data used in this work and the corresponding results are given in Section 2. The results of the multi-wavelength studies are shown in Section 3 and the origin of the γ -ray emissions are discussed in Section 4.

2. LHAASO DATA ANALYSIS AND RESULTS

LHAASO is a hybrid, large area, wide field-of-view extensive air shower array for the study of CRs and γ -rays in the sub-TeV to PeV energy range. It consists of three detector arrays: the 78000-m 2 Water Cherenkov Detector Array (WCDA), the 1.3-km 2 Kilometer Square Array (KM2A), and the Wide Field-of-view Cherenkov Telescope Array. WCDA is sensitive to γ -rays at energies between 100 GeV and 30 TeV (Ma et al. 2022), and KM2A operates from ~ 20 TeV to a few PeV (Aharonian et al. 2021a). LHAASO started partial operation in April 2019 and has been in full scientific operation since July 2021. More details about the experiment can be found in Aharonian et al. (2021a,b).

The LHAASO data used in this analysis are collected with WCDA and KM2A (see Table 1). According to the number of hits (N_{hit}), events recorded by WCDA are divided into five bins: 100–200, 200–300, 300–500,

Table 1. LHAASO observation data.

| Array | Time Period (yyyy.mm.dd) | Livetime (days) |
|-----------|--------------------------|-----------------|
| Full WCDA | 2021.03.05–2023.07.31 | 796 |
| 1/2 KM2A | 2019.12.27–2020.11.30 | 289.5 |
| 3/4 KM2A | 2020.12.01–2021.07.19 | 215.8 |
| Full KM2A | 2021.07.20–2023.07.31 | 710.7 |

500–800, and 800–2000, roughly corresponding to an energy range of 1 to 25 TeV. The $\mathcal{P}_{\text{inccness}}$ parameter improved from the original definition (Abeysekara et al. 2017) is used to exclude the CR background. Events with $\mathcal{P}_{\text{inccness}} < 1.1$ are used for this analysis. Events recorded by KM2A are divided into equally logarithmic energy bins with bin width $\Delta \log_{10} E_{\gamma} = 0.2$ and range from 25 TeV to several PeV. We adopt the pipeline of KM2A data analysis presented in Aharonian et al. (2021a) with the same event selection conditions.

The sky in the region of interest (ROI) is binned into cells with a size of 0.1° and filled with detected events according to their reconstructed arrival directions for each energy bin. The ‘direct integration method’ (Fleysher et al. 2004) is adopted to estimate the number of the CR background events. As for the modelling of the Galactic diffuse emission (GDE), we use the same templates as that in Cao et al. (2024). Dust column density measured by the PLANCK satellite (Planck Collaboration et al. 2014, 2016) is taken as the intensity template of GDE.

The significance map in the ROI is estimated using a test statistic (TS) variable as $\text{TS} = 2 \ln(\mathcal{L}/\mathcal{L}_0)$, where \mathcal{L} is the maximum likelihood of a point source signal plus background hypothesis and \mathcal{L}_0 is the maximum likelihood of the background only hypothesis. Assuming a power-law (PL) spectrum, the test source has an index of 2.6 in the energy range of 1–25 TeV and 3.0 at energies above 25 TeV. The detection significance usually can be simplified as the square root of the TS (Wilks 1938). To describe the γ -ray emission observed above 1 TeV, we fit both the WCDA and the KM2A data with a three-dimensional binned maximum likelihood method, which can determine the morphological and spectral parameters of multiple sources simultaneously. Since the GDE is position-dependent due to the variation of column density and CR density across the Galaxy, we only fix the GDE morphology to be the same as that in Cao et al. (2024) but set the normalization factor and spectral index of the GDE component as free parameters during the fitting process.

2.1. WCDA analysis and results

For the WCDA data, we analyse a $4^{\circ} \times 4^{\circ}$ square region centred at R.A. = 284.5° , Dec = 2.1° in the

celestial coordinate system. Figure 1(a) shows the background TS map in the ROI. The WCDA components of five extended 1LHAASO catalogue sources (1LHAASO J1858+0330, 1LHAASO J1857+0203u, 1LHAASO J1857+0245, 1LHAASO J1852+0050u, and 1LHAASO J1850–0004u) may contribute to the γ -ray emission within the ROI. Their positions and extensions resolved in the catalogue are displayed in Figure 1(a) with black dashed circles. The extension size of the source is described by a 2D-Gaussian r_{39} , corresponding to 39% of the measured events. They all have 2D-Gaussian morphologies and PL-type spectra. We also display the positions of the TeV or multi-TeV sources detected by H.E.S.S., MAGIC, and HAWC in Figure 1. We note that 1LHAASO J1857+0203u is spatially coincident with HESS J1858+020 and thus consider it our target source. We fit the positions, extensions, and spectral parameters of all five LHAASO sources simultaneously. The spectral parameters of the GDE are also set free. Table 2 summarises the optimised spatial parameters for the five LHAASO sources, shown as black solid circles in Figure 1(a).

We estimate the statistical position uncertainty, $\sigma_{\text{p},95,\text{stat}}$, at the 95% confidence level using the same method as that in Cao et al. (2024). Considering the pointing error only, the systematic positional uncertainty is estimated to be 0.04° (Cao et al. 2024). To test the extended nature of the target source, we calculate the TS value in terms of the likelihood ratio between the best-fit extended model (\mathcal{L}_{ext}) and the point source hypothesis (\mathcal{L}_{ps}), defined as $\text{TS}_{\text{ext}} = 2 \ln(\mathcal{L}_{\text{ext}}/\mathcal{L}_{\text{ps}})$. When determining the extension of the source, a systematic bias caused by the point spread function (PSF) measurement is conservatively estimated to be $\sim 0.05^{\circ}$ (Cao et al. 2024). Since the TS_{ext} obtained is 28.4 (5.3σ), we consider 1LHAASO J1857+0203u an extended source in 1–25 TeV. It has a statistical significance of 15.2σ and is centred at R.A. = $284.53^{\circ} \pm 0.08_{\text{stat}}^{\circ} \pm 0.04_{\text{sys}}^{\circ}$, Dec = $1.99^{\circ} \pm 0.09_{\text{stat}}^{\circ} \pm 0.04_{\text{sys}}^{\circ}$ with an extension of $r_{39} = 0.18^{\circ} \pm 0.03_{\text{stat}}^{\circ} \pm 0.05_{\text{sys}}^{\circ}$. These results are consistent with those reported in the 1LHAASO catalogue. Especially, the r_{39} extension circle covers the γ -ray excess measured by MAGIC in this region (see MAGIC Collaboration et al. 2014, Fig. 2), as well as the H.E.S.S. and HAWC sources.

The spectrum of the WCDA component of 1LHAASO J1857+0203u shows no curvature and is well fitted with a single PL: $dN/dE_{\gamma} = N_0 \times (E_{\gamma}/E_0)^{-\Gamma}$, with an index of $\Gamma = 2.46 \pm 0.09_{\text{stat}}$ and a differential flux normalization parameter $N_0 = (1.53 \pm 0.36_{\text{stat}}) \times 10^{-13} \text{ cm}^{-2} \text{ s}^{-1} \text{ TeV}^{-1}$ at $E_0 = 3 \text{ TeV}$. The derived photon index is consistent with the previous estimate by

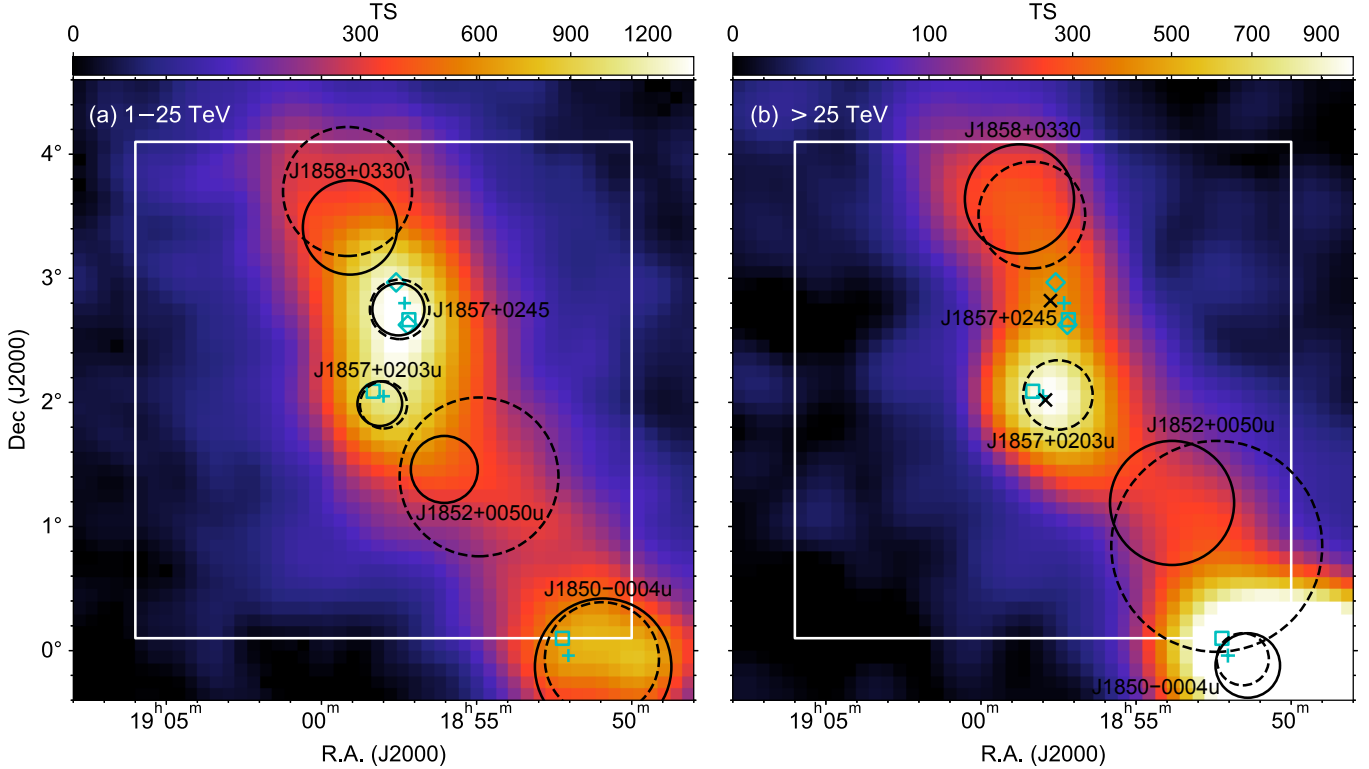


Figure 1. LHAASO TS maps of a $5^\circ \times 5^\circ$ region around 1LHAASO J1857+0203u. The white box indicates the ROI. The black dashed circles show the WCDA or KM2A components resolved in the first LHAASO catalogue. The cyan markers show the positions of potential TeV or multi-TeV counterparts detected by H.E.S.S. (box), MAGIC (diamond), and HAWC (cross). (a) WCDA TS map ($1 < E_\gamma < 25$ TeV). The black solid circles (with radii of r_{39} extensions) show the WCDA components resolved in this work. (b) KM2A TS map ($E_\gamma > 25$ TeV). The black crosses (corresponding to point-like sources) and black solid circles (with radii of r_{39} extensions) show the KM2A components resolved in this work.

Table 2. Optimised parameters of the WCDA and the KM2A components in the source model.

| 1LHAASO Sources ^a | Component | R.A. | Dec | Extension ^b | Potential TeV/GeV Counterparts |
|------------------------------|-----------|--------------|--------------|------------------------|--|
| | | ($^\circ$) | ($^\circ$) | ($^\circ$) | |
| 1LHAASO J1858+0330 | WCDA | 284.77 | 3.41 | 0.38 | 4FGL J1858.0+0354, |
| | KM2A | 284.69 | 3.64 | 0.44 | 4FGL J1900.4+0339 |
| 1LHAASO J1857+0245 | WCDA | 284.38 | 2.75 | 0.21 | MAGIC J1857.6+0297, MAGIC J1857.2+0263, |
| | KM2A | 284.44 | 2.82 | – | HESS J1857+026, 3HAWC J1857+027, 4FGL J1857.7+0246e |
| 1LHAASO J1857+0203u | WCDA | 284.53 | 1.99 | 0.18 | HESS J1858+020, xHWC J1858+020, |
| | KM2A | 284.48 | 2.02 | – | 4FGL J1858.3+0209 (SrcB) 4FGL J1857.6+0212 (SrcA) |
| 1LHAASO J1852+0050u | WCDA | 284.01 | 1.46 | 0.27 | 4FGL J1855.9+0121e, |
| | KM2A | 283.46 | 1.19 | 0.50 | 4FGL J1852.4+0037e |
| 1LHAASO J1850–0004u | WCDA | 282.73 | –0.13 | 0.55 | HESS J1852–000, xHWC J1852+000, |
| | KM2A | 282.85 | –0.12 | 0.26 | 4FGL J1851.8–0007c |

Notes.

^a The source names are consistent with those in the 1LHAASO catalogue.

^b The respective 39%-containment radii.

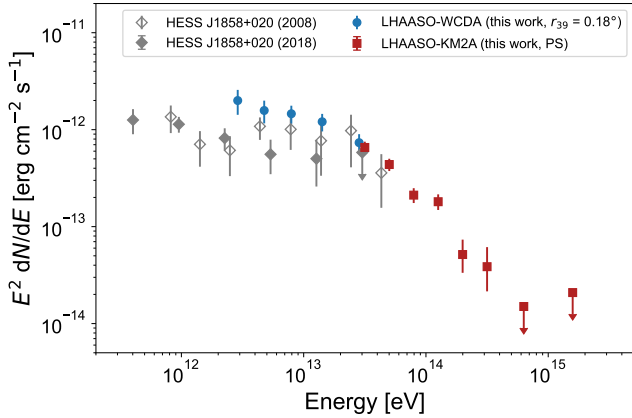


Figure 2. Differential energy spectrum of the TeV source 1LHAASO J1857+0203u. The blue dots and red squares represent the WCDA and KM2A data measured in this work, respectively. The combinations of statistics and systematic errors are shown. The 95% confidence upper limits are displayed with downward arrows. The grey diamonds show the H.E.S.S. flux data points (Aharonian et al. 2008; H. E. S. S. Collaboration et al. 2018).

H.E.S.S., $\Gamma = 2.2 \pm 0.1_{\text{stat}} \pm 0.2_{\text{sys}}$ (Aharonian et al. 2008) or $\Gamma = 2.39 \pm 0.12_{\text{stat}}$ (H. E. S. S. Collaboration et al. 2018). We extract the spectral energy distribution (SED) in the five N_{hit} bins. In each bin, we only fit the normalization parameters in the source model. As in Cao et al. (2024), the systematic uncertainty is estimated to be $\sim 8\%$ on the flux for the WCDA SED measurement. We also estimate the uncertainty caused by the imperfection model of the GDE with its spectral parameters fixed to the same values as those in the catalogue (Cao et al. 2024). The result shows an effect of less than 14% on the flux. The flux data points are shown in Figure 2. Since the extension measured by WCDA differs from the integration radius used in the H.E.S.S. spectrum measurement (0.15°), the flux points we obtained are slightly higher than those in Aharonian et al. (2008) but are consistent within the uncertainty range. The difference between the measurements of WCDA and H. E. S. S. Collaboration et al. (2018) may be ascribed to the peculiarity of the background subtraction in the H.E.S.S. Galactic plane survey analysis. HESS J1858+020 is located in a large exclusion region, the background could not be well constrained, which consequently resulted in the spectrum measurement that was not well constrained (H. E. S. S. Collaboration et al. 2018). In our SED modelling (see Section 4), only the H.E.S.S. data points published in 2008 are included.

2.2. KM2A analysis and results

For the KM2A data, the same ROI as that used for WCDA is selected. Figure 1(b) shows the background

TS map in the ROI. Of the five 1LHAASO catalogue sources mentioned in Section 2.1, all but 1LHAASO J1857+0245 have KM2A components. Their positions and extensions resolved in the catalogue are displayed in Figure 1(b) with black dashed circles. As a null hypothesis (denoted as $M0$), we add the four KM2A components and the GDE component in the source model. As for the test models, since 1LHAASO J1857+0245 is only $\sim 0.7^\circ$ away from the ROI centre, and its potential KM2A component may affect the fitting results, we add a fifth source as its KM2A component. To compare with the catalogue results, we first fix the parameters of the GDE component to the same values as those in the catalogue during the fitting processes, while the parameters of the other sources are set free. Considering the morphology (point-like/2D-Gaussian) of the target source (1LHAASO J1857+0203u) and the added source (1LHAASO J1857+0245), we test four models ($M1$ – $M4$, see Table 3), in which all the sources are assumed to have PL-type spectra.

We use the Akaike Information Criterion (AIC; Akaike 1974; Lande et al. 2012) to select the best-fit spatial model. AIC is defined as $\text{AIC} = 2k - 2 \ln \mathcal{L}$, where k is the number of free parameters in the model and \mathcal{L} is the likelihood of the model tested in the analysis. The model that minimizes the AIC is considered to be the best. Compared with the $M0$ model, the ΔAIC values of the models are shown in Table 3. Since the extended nature of 1LHAASO J1857+0203u and 1LHAASO J1857+0245 is not significant ($\text{TS}_{\text{ext}} < 9$), we consider them to be point-like at energies above 25 TeV. Then, considering the GDE effects on the morphology and the flux of the sources, we free the spectral parameters of the GDE component and repeat the fit (denoted as $M5$ – $M8$). Still, the extended nature of the two sources is not significant. Compared to the $M1$ model, the $M5$ model shows an improvement of 3.5σ ($\text{TS} = 15.0$). Therefore, the best-fit results of the $M5$ model are used in our analysis.

The KM2A component of 1LHAASO J1857+0203u has a statistical significance of 21.4σ at energies above 25 TeV and is centred at $\text{R.A.} = 284.48^\circ \pm 0.05_{\text{stat}}^\circ \pm 0.03_{\text{sys}}^\circ$, $\text{Dec} = 2.02^\circ \pm 0.05_{\text{stat}}^\circ \pm 0.03_{\text{sys}}^\circ$. The statistical position uncertainty $\sigma_{\text{p},95,\text{stat}}$ is estimated and the systematic positional uncertainty is estimated to be 0.03° when the pointing error is considered (Cao et al. 2024). The upper limit on the extension at the 95% confidence level is 0.18° , which is compatible with the WCDA result. Table 2 summarises the optimised spatial parameters and the potential TeV or GeV counterparts of the five LHAASO sources. In our analysis, the KM2A component added for 1LHAASO J1857+0245 has a TS value

of 64 at energies above 25 TeV, indicating a new source. Given that, 1LHAASO J1852+0050u and 1LHAASO J1850–0004u are labelled as doubtful merging sources in the 1LHAASO catalogue, and 1LHAASO J1852+0050u and 1LHAASO J1858+0330 are affected by the GDE significantly, it is understandable that their parameters deviate from the catalogue results. Detailed analysis about these sources will be published separately.

Figure 3 shows the $1^\circ \times 1^\circ$ TS map around 1LHAASO J1857+0203u at energies above 100 TeV, smoothed by the corresponding PSF. The TS value for 1LHAASO J1857+0203u above 100 TeV is 134, corresponding to a statistical significance of 11.6σ . The positions of the WCDA and KM2A components of 1LHAASO J1857+0203u are consistent with the TeV sources xHWC J1858+020 and HESS J1858+020 within statistical uncertainties. The GeV source SrcB overlaps the north of HESS J1858+020 and is possibly the GeV counterpart of the TeV sources.

The spectrum of the KM2A component of 1LHAASO J1857+0203u also shows no curvature and is well described by a simple PL with an index $\Gamma = 3.22 \pm 0.10_{\text{stat}}$ and a differential flux normalization parameter $N_0 = (1.00 \pm 0.07_{\text{stat}}) \times 10^{-16} \text{ cm}^{-2} \text{ s}^{-1} \text{ TeV}^{-1}$ at $E_0 = 50 \text{ TeV}$. The SED is extracted in eight logarithmically spaced energy bins. Specifically, the width of the last two energy bins (above 400 TeV) is $\Delta \log_{10} E_\gamma = 0.4$. In each energy bin, only the normalization parameters are fitted. If the TS value of the source in a bin is less than 4, the 95% confidence upper limit of its flux is estimated. As in Aharonian et al. (2021a), the systematic uncertainty mainly comes from the atmospheric model used in the Monte Carlo simulation. In this case, the systematic uncertainty is estimated to be $\sim 7\%$ on the flux and 0.02 on the spectral index for the KM2A SED measurement. The uncertainty caused by the imperfection model of the GDE is also calculated by comparing the *M1* and *M5* models, resulting in a deviation of less than 5%. Figure 2 shows the differential energy spectrum of the γ -ray emission obtained in this work. We note that the spectrum of the KM2A component can be well connected with the WCDA component and that the non-detection of extension by KM2A does not contradict the WCDA results, indicating that they are likely of the same origin.

3. MULTI-WAVELENGTH STUDIES

3.1. Molecular environment

To investigate the potential molecular gases that may contribute to the hadronic emission, we use the archival CO data of the FOREST Unbiased Galactic plane Imaging survey with the Nobeyama 45 m telescope (FUGIN;

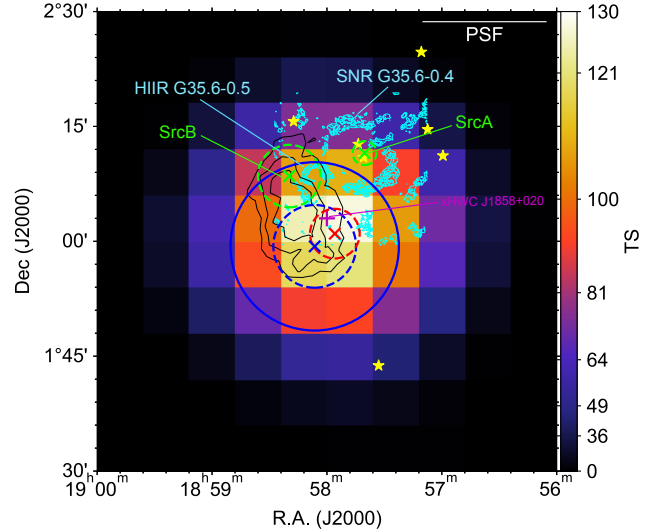


Figure 3. TS map of a $1^\circ \times 1^\circ$ region around 1LHAASO J1857+0203u as observed by LHAASO above 100 TeV. The blue and red crosses with σ_{95} statistical position error circles (dashed) show the WCDA and KM2A components resolved in this work, respectively. The solid blue circle marks the r_{39} extension circle of the WCDA component. The green crosses with σ_{95} statistical position error circles (dashed) show the GeV γ -ray point-like sources (SrcA & SrcB) detected by Zhang et al. (2022). The magenta cross (‘+’) represents the position of the UHE γ -ray point-like source detected by HAWC (Malone et al. 2023). The yellow stars represent the PSRs located within a radius of 0.5° from the TeV source. The black contours show the TeV source HESS J1858+020 with 5σ , 6σ , and 7σ significance (H. E. S. S. Collaboration et al. 2018). The cyan contours indicate the GMRT 610 MHz radio emission (Paredes et al. 2014), where the larger shell-like structure corresponds to SNR G35.6–0.4 and the smaller ring-shaped structure corresponds to HIR G35.6–0.5. The line segment at the top-right corner shows the size of the PSF (68% containment).

Umemoto et al. 2017) observation. The data has an angular resolution of $20''$ and an average RMS of 1.5 K at a velocity resolution of 0.65 km s^{-1} . Figure 4 shows the spatial distribution of the ^{12}CO ($J=1-0$) emission in velocity range $\sim +50$ to $+68 \text{ km s}^{-1}$, with velocity intervals 2 km s^{-1} . Some molecular clumps appear in morphological agreement with the detected TeV γ -ray emissions. As shown in Figure 4, we denote the clumps in two box regions as ‘W’ and ‘K’. The centre positions and sizes of the clouds are listed in Table 4. When estimating the molecular column density and the mass of the molecular gas, local thermodynamic equilibrium for the molecular gas and optically thick conditions for the ^{12}CO ($J=1-0$) line are assumed. The excitation temperature is calculated with $T_{\text{ex}} = 5.53/\ln[1 + 5.53/(T_{\text{peak}}(^{12}\text{CO}) + 0.819)] \text{ K}$ (Nagahama et al. 1998), where $T_{\text{peak}}(^{12}\text{CO})$ is the peak tem-

Table 3. Δ AIC results for different spatial model combinations used for the KM2A analysis.

| Models | 1LHAASO J1857+0203u | 1LHAASO J1857+0245 | GDE ^a | Δk ^b | Δ AIC ^b |
|-----------|---------------------|--------------------|------------------|-------------------------|---------------------------|
| <i>M0</i> | 2D-Gaussian | – | fixed | 0 | 0 |
| <i>M1</i> | point-like | point-like | fixed | 3 | –20.2 |
| <i>M2</i> | point-like | 2D-Gaussian | fixed | 4 | –18.8 |
| <i>M3</i> | 2D-Gaussian | point-like | fixed | 4 | –25.0 |
| <i>M4</i> | 2D-Gaussian | 2D-Gaussian | fixed | 5 | –23.4 |
| <i>M5</i> | point-like | point-like | free | 5 | –31.2 |
| <i>M6</i> | point-like | 2D-Gaussian | free | 6 | –29.4 |
| <i>M7</i> | 2D-Gaussian | point-like | free | 6 | –36.4 |
| <i>M8</i> | 2D-Gaussian | 2D-Gaussian | free | 7 | –34.4 |

Notes.

^a The spectral parameters of the GDE component are fixed to the same values as those in the catalogue (Cao et al. 2024) in *M0–M4* but free in *M5–M8*.

^b k and AIC values are provided as differences with respect to the *M0* model.

perature of the maximum ^{12}CO ($J=1-0$) emission point in the cloud region. The column density is calculated via $N(\text{H}_2) = 1.49 \times 10^{20} W(^{13}\text{CO}) / [1 - \exp(-5.29/T_{\text{ex}})] \text{ cm}^{-2}$ (Nagahama et al. 1998), where $W(^{13}\text{CO})$ is the integrated intensity of the ^{13}CO ($J=1-0$) line in the velocity range $\sim +50$ to $\sim +70 \text{ km s}^{-1}$. The abundance ratio $[\text{H}_2]/[^{13}\text{CO}]$ is taken as 7×10^5 (Frerking et al. 1982). After estimating the $N(\text{H}_2)$ value in each pixel of the corresponding regions, the average values for the clouds are obtained. The relation $M = 2.8 m_{\text{H}} N(\text{H}_2) A$ is then used to derive the mass of the molecular gas, where m_{H} is the mass of a hydrogen atom and A is the cross-sectional area of the corresponding clouds. For comparison, both the near ($\sim 3.4 \text{ kpc}$) and far ($\sim 10.5 \text{ kpc}$) distances (Zhang et al. 2022) are used in the estimation. The clouds are simply approximated as cubes when calculating the average number densities of hydrogen nuclei (n_{H}). The derived parameters of the molecular clouds are summarised in Table 4.

3.2. Atomic clouds

To estimate the parameters of the atomic clouds that may be associated with the γ -ray emissions, we obtain the 1420 MHz HI line emission data from the Very Large Array Galactic Plane Survey (Stil et al. 2006). The synthesized beam for the HI spectral line images is $18''$ and the radial velocity resolution is 0.824 km s^{-1} . Figure 5 shows the column density map of the HI line emission calculated in the velocity range of $+50$ – $+70 \text{ km s}^{-1}$. The atomic hydrogen column density is measured using an HI intensity-mass conversion factor of $X_{\text{HI}} = 1.823 \times 10^{18} \text{ cm}^{-2} / (\text{K km s}^{-1})$ (Rohlfs & Wilson 2004). The centre gases appear to be spatially consistent with the detected TeV γ -ray emissions. We mark the gases in a box region as ‘A’ (see Figure 5), of which the centre position and size are listed in Table 4. Similar to the estimation methods in Section 3.1, the average

column density, mass, and number density of hydrogen nuclei for cloud ‘A’ are also obtained and summarised in Table 4.

3.3. Search for OB stars

It is suggested that particles can be accelerated by the colliding winds of young massive clusters (Aharonian et al. 2019) which are the ionizing sources of HIIRs. O- and B-type (OB) stars are massive stars that have strong stellar winds. To find massive stars (OB stars) that may be associated with HIIR G35.6–0.5, we first search in the OB-star candidate catalogue selected from the VST Photometric H α Survey data release 2 (VPHAS+ DR2) (Chen et al. 2019) and the available catalogue of all O-B2 stars compiled from the literature (Chen et al. 2019) but obtain no results. Then, we select all sources from the *Gaia* DR3 database (the `gaia_source` table, Gaia Collaboration et al. 2016, 2023a) in a $0.5^\circ \times 0.5^\circ$ area, centred on R.A. = 284.50° , Dec = 2.05° (see the green box in the middle left panel of Figure 4). Then we select the stars that received a `spectraltype_esphs` tag \in [‘O’, ‘B’] in the `astrophysical_parameters` table (Gaia Collaboration et al. 2023b), and fix the effective temperature T_{eff} threshold at 9000 K. After filtering, 26 sources remained in the list of candidate-OB stars. Among these, seven sources are distributed in a distance (d) range between 2.8 kpc and 4.0 kpc, which covers the near kinematic distance of HIIR G35.6–0.5 ($3.4 \pm 0.4 \text{ kpc}$). For a further constraint, we consider the sources with absolute G magnitude $M_G = G - 5(\log_{10} d - 1) - A_G < 0$ (Chen et al. 2019), where A_G is the interstellar extinction. This results in a total of six candidate-B stars (see Table 5 and Figure 4), among which four are in the `gold_sample_oba_stars` table (Gaia Collaboration et al. 2023b). Unfortunately, the candidates appear scattered, and none are near the centre of HIIR G35.6–0.5. These isolated candidate-B stars are incapable of accelerating

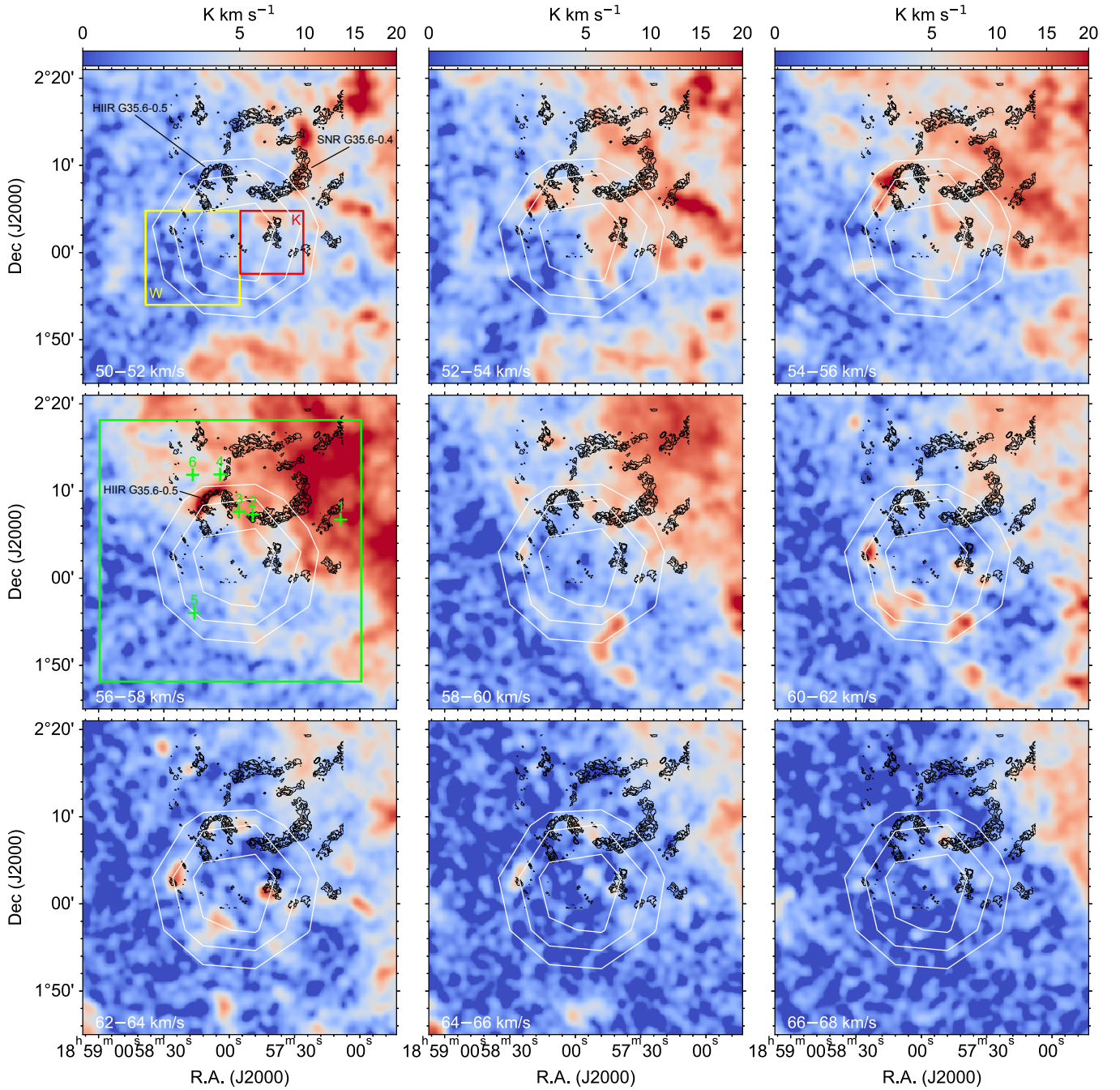


Figure 4. Spatial distribution of the MCs. FUGIN ^{12}CO ($J=1-0$) intensity maps integrated each 2 km s^{-1} in the velocity range $+50$ – $+68\text{ km s}^{-1}$, overlaid with black contours of GMRT 610 MHz radio emission (same as the cyan contours in Fig. 3) and white TS contours for 1LHAASO J1857+0203u above 100 TeV at levels of 100, 110, and 120. The yellow and red boxes marked with ‘W’ and ‘K’ in the top left panel show the regions that are used to estimate the parameters of the $+50$ – $+70\text{ km s}^{-1}$ molecular gases. The green box in the middle left panel ($+56$ – $+58\text{ km s}^{-1}$, corresponds to a near distance of $3.4 \pm 0.4\text{ kpc}$) marks the region where we search for OB stars, and the green crosses mark the positions of the OB star candidates.

Table 4. Properties of the molecular and atomic clouds.

| Clouds | (R.A., Dec) ^a (°) | Size (°) | $N(\text{H}_2)$ or $N(\text{HI})$ (10^{21} cm^{-2}) | d (kpc) | M ($10^3 M_\odot$) | n_{H} (cm^{-3}) | T_{ex} (K) |
|--------|---------------------------------|-------------|--|--------------|---------------------------|--|------------------------|
| W | (284.57, 1.99) | 0.18 | 1.6 | 10.5 | 39.3 | 30 | 23.4 |
| | | | | 3.4 | 4.1 | 100 | |
| K | (284.42, 2.02) | 0.12 | 2.0 | 10.5 | 21.5 | 60 | 18.8 |
| | | | | 3.4 | 2.3 | 180 | |
| A | (284.53, 1.99) | 0.26 | 3.0 | 10.5 | 76.3 | 20 | – |
| | | | | 3.4 | 8.0 | 60 | |

Notes.^a centre of the cloud.**Table 5.** Candidate-B stars around HIR G35.6–0.5.

| No. | ID | (R.A., Dec) (°) | G (mag) | A_G (mag) | BP (mag) | RP (mag) | Parallax (mas) | Distance (pc) | T_{eff} (K) |
|-----|---------------------|------------------------|--------------|----------------|---------------|---------------|-------------------|------------------|-------------------------|
| 1 | 4267138008163989376 | (284.289202, 2.109622) | 15.44 | 3.32 | 16.33 | 14.49 | 0.608 ± 0.038 | 3383.17 | 9142.34 |
| 2 | 4268591631256410368 | (284.457488, 2.119467) | 15.36 | 3.38 | 16.26 | 14.41 | 0.481 ± 0.035 | 3306.22 | 9267.10 |
| 3 | 4268591974853788544 | (284.483678, 2.124783) | 16.03 | 3.66 | 16.98 | 14.98 | 0.578 ± 0.137 | 3877.79 | 9386.42 |
| 4 | 4268640731323327488 | (284.519704, 2.196094) | 15.41 | 2.91 | 16.16 | 14.56 | 0.549 ± 0.034 | 3755.30 | 9198.58 |
| 5 | 4267084368314521088 | (284.569054, 1.931037) | 15.32 | 3.30 | 16.20 | 14.38 | 0.517 ± 0.029 | 3514.04 | 9039.63 |
| 6 | 4268594139517304448 | (284.572168, 2.195489) | 15.34 | 2.93 | 16.08 | 14.48 | 0.550 ± 0.034 | 3152.76 | 9130.34 |

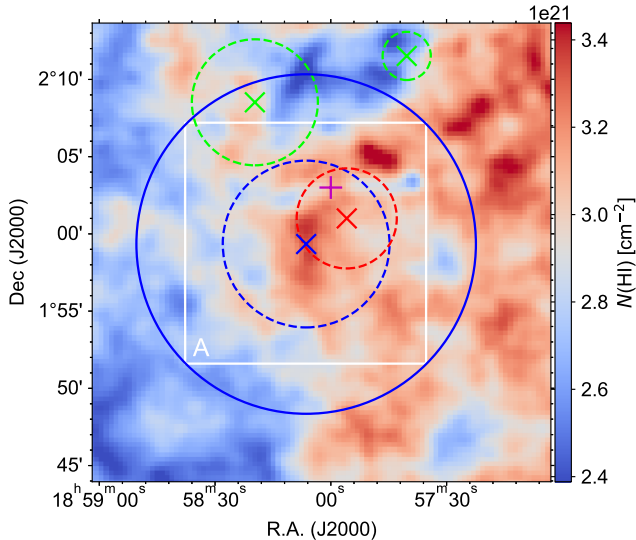


Figure 5. HI column density map calculated in the velocity range of $+50$ – $+70$ km s^{-1} . The crosses and circles are the same as those in Figure 3. The white box marked with ‘A’ shows the region used to estimate the parameters of the $+50$ – $+70$ km s^{-1} atomic gases.

CRs to high energies. We also investigate the *Gaia* colour-absolute magnitude diagram, as well as other observations, such as VPHAS+ DR3 and 2MASS, but no positive results appear. We therefore conclude that, based on the data available to date, no OB associations or massive star clusters have been found to be associated with HIIR G35.6–0.5.

3.4. Radio and X-ray observations

We explore the radio observations towards the 1LHAASO J1857+0203u region with the survey data: the 1–2 GHz HI/OH/Recombination line survey (THOR; Beuther et al. 2016; Wang et al. 2020) combined with the Very Large Array Galactic Plane Survey (VGPS; Stil et al. 2006), which is called the THOR+VGPS¹, and the Effelsberg 11 cm (~ 2.7 GHz) survey of the Galactic plane by Reich et al. (1984)². No significant radio emissions were detected in the central region of 1LHAASO J1857+0203u at 1.4 GHz and 2.7 GHz. We estimate the upper limits of the flux densities for a source with a radius of 0.18° ($= r_{39}$) centred at R.A. = 284.53° , Dec = 1.99° . To remove the contamination from HIIR G35.6–0.5 and SNR G35.6–0.4 we first calculate a circular region with a radius of 0.09° ($0.5r_{39}$) and then scale the results. The 2σ upper limits

of the flux densities at 1.4 GHz and 2.7 GHz are 65.5 Jy and 25.3 Jy, respectively.

Paredes et al. (2014) analysed the *Chandra* X-ray (0.4–7 keV) data in the HESS J1858+020 region and found no extended X-ray emission. They obtained the 2σ upper limit to be $\sim 1 \times 10^{-13} \text{ erg cm}^{-2} \text{ s}^{-1}$ for a source with a $6' \times 6'$ extension and an X-ray spectrum of a PL of photon-index $\Gamma = 2$, based on the statistical fluctuation of the background of the field. Here we scale the result to the r_{39} extension of 1LHAASO J1857+0203u and obtain $\sim 1 \times 10^{-12} \text{ erg cm}^{-2} \text{ s}^{-1}$. No other X-ray telescopes have observed or detected emission in this region.

4. DISCUSSION

In the above LHAASO data analysis, we found that 1LHAASO J1857+0203u is an extended source in the WCDA band (1–25 TeV) which almost covers the TeV source HESS J1858+020 and the GeV source SrcB (see Figure 3). In the KM2A band (> 25 TeV), however, it is a point-like source and has an angular separation of 0.18° to SrcB, without overlap between the position error circles of them. Considering the position uncertainties, it is not easy to identify whether SrcB, HESS J1858+020, and 1LHAASO J1857+0203u have the same origin. If this is the case, as suggested in Zhang et al. (2022), HIIR G35.6–0.5 would be a likely source of the GeV/TeV–PeV γ -ray emissions. Meanwhile, 1LHAASO J1857+0203u projectively appears close to SNR G35.6–0.4, with an angular distance less than 0.2° . Hence, there is a possibility that 1LHAASO J1857+0203u is unrelated to SrcB but is produced by the illumination of MCs by the escaped protons from the SNR. In the latter case, SrcB would be an independent source associated with HIIR G35.6–0.5. Furthermore, given the deviations of the central positions of the GeV and TeV γ -ray sources, it is also possible that the TeV emission is neither associated with the HIIR nor the SNR. An undetected PWN scenario would then be considered. We searched the SIMBAD Astronomical Database (Wenger et al. 2000)³ and found no binary system or other plausible counterpart. Therefore, we discuss the above three scenarios in this section.

4.1. HII region scenario

Given the association of the GeV γ -ray position with the MCs around the HIIR G35.6–0.5 at the near distance ~ 3.4 kpc, Zhang et al. (2022) suggested the GeV–TeV spectral points that seem to be smoothly connected

¹ https://www2.mpia-hd.mpg.de/thor/Data_%26_Publications.html

² <https://www3.mpifr-bonn.mpg.de/survey.html>

³ <http://simbad.u-strasbg.fr/simbad/sim-fcoo>

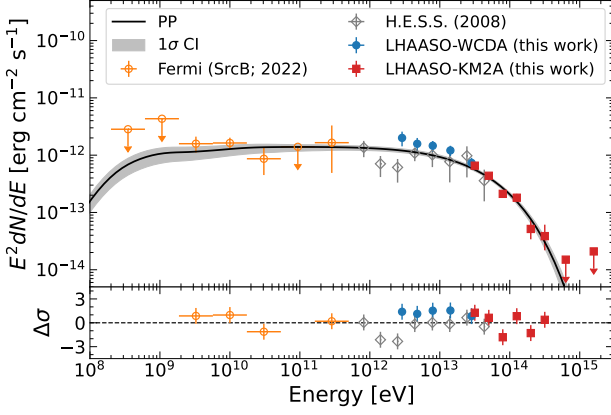


Figure 6. Fitted SED for the HII region scenario. The pion-decay γ -rays with 1σ confidence interval is represented by the black line. The Fermi data (orange circle) for SrcB are adopted from Zhang et al. (2022).

could be explained by a hadronic interaction. This notion is extended here to the combination of the *Fermi*-LAT GeV data, the WCDA TeV data, and the KM2A sub-PeV data. In this scenario, the γ -ray emissions from GeV to sub-PeV around the radio complex G35.6–0.4 are considered powered by a potential accelerator hidden in the HIIR G35.6–0.5. The WCDA component of 1LHAASO J1857+0203u and HESS J1858+020 are treated as the same γ -ray source, and the SrcB and the KM2A component are the GeV and sub-PeV counterparts, respectively.

We assume the accelerated protons have a PL distribution in energy with an exponential cutoff $E_{p,\text{cut}}$: $dN_p/dE_p \propto E_p^{-\alpha_p} \exp(-E_p/E_{p,\text{cut}})$, where E_p is the particle energy, and α_p is the PL index. The normalization is determined by the total energy in particles with energies above 1 GeV, W_p . We use the *Naima* package (version 0.9.1, Zabalza 2015) to fit the GeV–PeV energy spectrum. In the fitting process, the γ – γ absorption is not considered due to the negligible influence on the flux for the distance of 3.4 kpc (see Appendix A). By adopting an average atomic hydrogen number density $n_t \sim 600 \text{ cm}^{-3}$ of the target gas for the p-p interaction (Zhang et al. 2022), we obtain $\alpha_p = 2.04_{-0.05}^{+0.04}$, $E_{p,\text{cut}} = 445_{-67}^{+83} \text{ TeV}$, and $W_p = 1.34_{-0.25}^{+0.27} \times 10^{47} (n_t/600 \text{ cm}^{-3})^{-1} \text{ erg}$. The fitted SED is shown in Figure 6.

Although no massive stars have yet been detected in HIIR G35.6–0.5 (see Section 3.3), it cannot be ruled out that they are embedded in the MCs. Here we assume that the energetic protons are accelerated by the stellar winds of the massive stars and discuss the possibility from the energy budget side. The proton luminosity $L_p(> 1 \text{ GeV})$ can be roughly de-

rived from $\int_{1 \text{ GeV}}^{+\infty} E_p dN_p/dE_p / \min(\tau_{pp}, t_c) dE_p$, where τ_{pp} and t_c are the proton’s lifetime and confinement time, respectively. For the hadronic process, the lifetime is $\tau_{pp} = 10^5 (n_t/600 \text{ cm}^{-3})^{-1} \text{ yr}$. The confinement time can be estimated by $t_c = L^2/6D$ (Aharonian & Atoyan 1996), where L and D are the source physical size ($\sim 0.2^\circ$) and the diffusion coefficient, respectively. We assume that the diffusion coefficient has a general form $D = \chi 10^{28} (E_p/10 \text{ GeV})^\delta \text{ cm}^2 \text{ s}^{-1}$, where both χ and δ are dimensionless constant. The particular values of $\delta = 1/3$ and 1 correspond to the Kolmogorov- and Bohm-like diffusion regimes, respectively. For the CR propagation models, $\chi = 1$ and $\delta = 0.3$ – 0.6 are required (e.g. Berezhinskii et al. 1990). While recent observations suggest that the diffusion coefficient around the particle acceleration site may be significantly lower than the average value in Galaxy, giving $\chi \leq 0.01$ (e.g. Fujita et al. 2010; Ohira et al. 2011; Li & Chen 2012; Abeyssekara et al. 2017). Considering this fact, the injection luminosity of protons is $L_p \sim (4\text{--}50) \times 10^{35} (\chi/0.01) (L/10 \text{ pc})^{-2} \text{ erg s}^{-1}$ for $\delta = 0.3$ – 0.6 . For a typical OB-type star, it has a strong stellar wind with a mass loss rate of order $10^{-6} M_\odot \text{ yr}^{-1}$ and a velocity of order 10^3 km s^{-1} , giving total mechanical energy in wind $\sim 10^{35} \text{ erg s}^{-1}$. Assuming that a fraction $\eta_w \sim 10\%$ of the mechanical energy is used to accelerate protons, the required number of massive stars is $N \sim 40\text{--}500 (\eta_w/0.1)^{-1} (\chi/0.01) (L/10 \text{ pc})^{-2}$. This star number within a region of $\sim 10 \text{ pc}$ can be satisfied in the young massive star clusters or associations with a typical radius of a few pc and 10^3 – 10^6 stars (Portegies Zwart et al. 2010). For instance, there are ~ 300 stars with a mass above $15 M_\odot$ for a young massive star cluster with a total mass of $10^5 M_\odot$ and a Salpeter-like mass function (Salpeter 1955) in the mass range from 0.1 to $100 M_\odot$. Thus deep searches for OB stars in this region are still needed. If there are enough massive stars and/or strong suppression of the diffusion coefficient, the stellar winds could supply the required energy to accelerate particles.

A number of protostars, with at least one among them possibly of high mass nature, were found in HIIR G35.6–0.5 (Paron & Giacani 2010; Paron et al. 2011). Although no signature of outflows was confirmed (Paron et al. 2011), the apparent elongation of the region may indicate a powerful outflow, which could be masked in radio by strong free-free absorption (Paredes et al. 2014). In addition, the elongated CO structure and several X-ray sources with positions roughly aligned with the former indicate that there is an active star-formation region (Paredes et al. 2014). The outflow and the entire star formation region could also be the origin of, or contribute to, the γ -ray emissions observed.

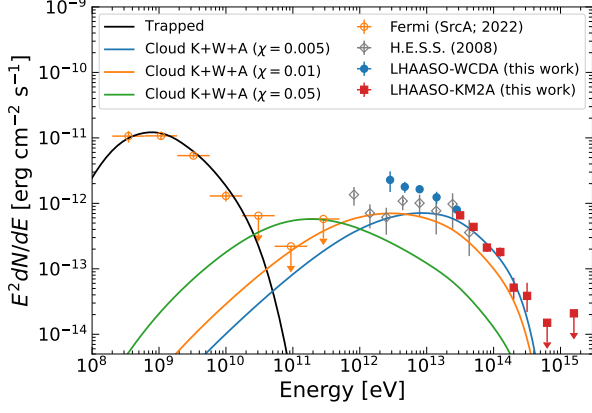


Figure 7. SED of the SNR scenario including the $\gamma - \gamma$ absorption. The black solid line represents the γ -rays from the trapped protons, which explains the GeV data of SrcA (Zhang et al. 2022). The γ -ray emission produced by the escaped protons is displayed in blue, orange, and green solid lines for $\chi = 0.005, 0.01, \text{ and } 0.05$, respectively.

4.2. Clouds illuminated by particles escaped from SNR

The second case is that the TeV–PeV γ -rays arise from the MCs around SNR G35.6–0.4 illuminated by the diffusing protons that escaped from the SNR shock wave. The estimated far kinematic distance of Clouds K, W, and A with $v_{\text{LSR}} \sim 60 \pm 10 \text{ km s}^{-1}$ is $\sim 10 \text{ kpc}$ (Wenger et al. 2018; Reid et al. 2014), which is very close to that of SNR G35.6–0.4 ($\sim 10.5 \text{ kpc}$, Zhang et al. 2022). Thus, there is a possibility that the three clouds are at the same distance as the SNR and are located in the vicinity of the SNR. While some of the escaped protons illuminate the nearby non-contact clouds, the trapped protons at the current stage also can generate γ -ray emission via bombarding the interacting MCs, which may explain the GeV source SrcA in Zhang et al. (2022). We calculate the expected γ -ray fluxes according to the so-called isotropic delta-escape model described in Gabici et al. (2009) and compare them with the observational data. In the calculation, the $\gamma - \gamma$ absorption is included due to the large distance (see Appendix A).

The distribution function of escaped protons without energy losses at any given distance R from the SNR centre and at any given time t is (Atoyan et al. 1995; Gabici et al. 2009)

$$f_{\text{esc}}(E_p, R, t) = \frac{A_0 E_p^{-\alpha_p}}{\pi^{3/2} R_d^3} \exp\left(-\frac{R^2}{R_d^2}\right), \quad (1)$$

where α_p and E_p are the PL index and the proton energy, respectively. The normalization factor, A_0 , is derived from $\eta E_{\text{SN}} = \int_{1 \text{ GeV}}^{E_{p,\text{max}}} E_p A_0 E_p^{-\alpha_p} dE_p$, where E_{SN} is the explosion energy, η is the energy conversion efficiency, and $E_{p,\text{max}}$ is the maximum energy of the ac-

celerated protons. The diffusion length is

$$R_d = \sqrt{4D(E_p)(t - t_{\text{esc}}(E_p))}, \quad (2)$$

where $t_{\text{esc}}(E_p) = t_{\text{sed}}(E_p/E_{p,\text{max}})^{-1/\mu}$ is the parameterised escape time when the protons of energy E_p escape from the SNR (Gabici et al. 2009) with t_{sed} the beginning time of the Sedov phase and μ a free parameter. In the above equation, $D(E_p)$ is the energy-dependent diffusion coefficient and the form in the CR propagation models $D(E_p) = \chi 10^{28} (E_p/10 \text{ GeV})^\delta$ with $\delta = 0.3 - 0.6$ (Berezinskii et al. 1990) is adopted here. The distribution of the protons confined in the SNR is

$$dN_p/dE_p = A_0 E_p^{-\alpha_p} \exp(-E_p/E_{p,\text{trap}}), \quad (3)$$

where $E_{p,\text{trap}} = E_{p,\text{max}}(t/t_{\text{sed}})^{-\mu}$.

Given the distribution of the escaped protons, the flux of the γ -ray emission from a cloud is

$$\frac{dN}{dE_\gamma} = \frac{M_c}{m_H} \frac{\epsilon_\gamma}{4\pi d^2}, \quad (4)$$

where M_c and m_H are the mass of the cloud and the mass of the hydrogen atom, respectively, ϵ_γ is the γ -ray emissivity per hydrogen atom and is calculated based on the method developed by Kafexhiu et al. (2014).

SNR G35.6–0.4 almost has a circular shape in the sky plane with an average radius of 15 pc at a distance of 10.5 kpc. Although there are the associated MCs at the western boundary suggested by Zhang et al. (2022), the average ambient (or inter-cloud) density $n_0 \sim 1 \text{ cm}^{-3}$ is assumed to estimate the dynamical age. Assuming an explosion energy $E_{\text{SN}} = 10^{51} \text{ erg}$ and the ejecta mass $M_{\text{ej}} = 2 M_\odot$, the beginning time of the Sedov phase is $t_{\text{sed}} \sim 330 \text{ yr}$ and the SNR age can be estimated as $t_{\text{SNR}} \sim 16 \text{ kyr}$ based on the Sedov solution. The separation between Cloud K/W/A and the SNR centre is $9.6'/13.9'/13.1'$, corresponding to a projective distance of $\sim 29/43/40 \text{ pc}$, respectively. The true distance of clouds from the SNR centre should not be smaller than the projective distance. In our calculation, $R_K = 30 \text{ pc}$, $R_W = 45 \text{ pc}$, and $R_A = 45 \text{ pc}$ are adopted for the Cloud K, W, and A, respectively.

For the accelerated protons, we assume the index $\alpha_p = 2$, $\eta = 10\%$, and $E_{p,\text{max}} = 1 \text{ PeV}$. Then we apply the above escape model to the observational data. We first fit the GeV data of SrcA (see the black line in Figure 7), resulting in $\mu \approx 2.68$ and $n_t = 200 \text{ cm}^{-3}$. The fitted target density is consistent with the SNR-MC interaction scenario (Zhang et al. 2022). For $\mu \approx 2.68$, corresponding to $E_{p,\text{trap}} \sim 30 \text{ GeV}$ at the current SNR age, it means that the protons with energy below 30 GeV are still confined in the SNR region.

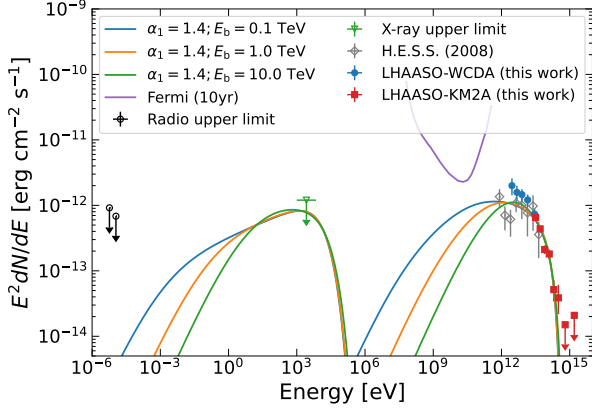


Figure 8. SED for the PWN scenario. The purple solid line shows the sensitivity of *Fermi*-LAT. The black and green data points are the radio and X-ray upper limits obtained in Section 3.4.

Then, the γ -ray emission from the nearby MCs illuminated by the escaped protons can be calculated, which is determined by two parameters δ and χ . In Figure 7, as an example, we display the expected γ -ray flux from Clouds K, W, and A with $\chi = 0.005$ (blue), 0.01 (orange), and 0.05 (green) for the Kolgomorov-type diffusion $\delta = 1/3$. The peak energy of SED can shift down to the TeV energies for larger χ , while the flux around ~ 100 TeV is suppressed. This is because the protons that produce ~ 100 TeV γ -rays have effectively passed through the cloud due to the larger diffusion coefficient (Aharonian & Atoyan 1996). In addition, δ and χ are degenerated, resulting in the same situation for other values of δ . As can be seen, the predicted γ -ray emission from the escaped protons can not explain the LHAASO data unless the nearby clouds have a larger mass (e.g. the mass of Cloud K is amplified by 4 times, see Appendix B). Therefore, the isotropic escape model can be ruled out due to the low total masses and/or the large separation from SNR of Clouds K, W, and A.

If the diffusion process is not isotropic, however, the required cloud mass can be smaller. For the bipolar diffusion in which the escaped protons diffuse from the SNR only within two cones and one happens to cover Clouds K, W, and A, the energy density of the protons can be roughly amplified by a factor of $10.7(\Omega/0.59)^{-1}$, where Ω is the solid angle of a cone and its apex angle 50° is adopted here.

4.3. PWN scenario

Apart from the two hadronic cases discussed above, there is another possible case, in which the TeV–PeV γ -rays arise from leptonic emission from PWNe. PWNe are efficient accelerators for the extremely relativistic

Table 6. Parameters used in the PWN scenario.

| α_1^a | E_b^a (TeV) | B^a (μ G) | α_2 | $E_{e,\text{cut}}$ (TeV) | W_e (10^{47} erg) |
|--------------|------------------|---------------------|------------|-----------------------------|---------------------------|
| 1.4 | 0.1 | 3 | 2.71 | 276 | 3.2 |
| 1.4 | 1.0 | 3 | 2.77 | 284 | 0.8 |
| 1.4 | 10.0 | 3 | 3.19 | 345 | 0.3 |

Notes.

^a Fixed in the fitting process.

leptons (electrons and positrons), and can generate the broadband electromagnetic wave from radio to UHE γ -rays via synchrotron and inverse Compton (IC) scattering. As a PWN evolves, the synchrotron flux (from radio to X-rays) decreases, whereas the IC flux (GeV–TeV γ -rays) increases until reaching a steady state value (de Jager et al. 2009). At a certain stage, PWNe can be only bright in γ -ray band and may be responsible for some unidentified TeV sources (de Jager et al. 2009). According to the Australia Telescope National Facility (ATNF; Manchester et al. 2005)⁴ Pulsar Catalogue, seven known PSRs are located within 0.5° from the LHAASO source emission centre. As shown in Figure 3, all the PSRs lie outside the WCDA r_{39} extension circle. It is possible that 1LHAASO J1857+0203u is powered by an undiscovered or putative PSR.

We assume that the distribution of the evolved leptons in PWN approximately have a smooth broken PL form with a high-energy cutoff (Zhang et al. 2020; Liu et al. 2024)

$$\frac{dN}{dE_e} = A_e E_e^{-\alpha_1} \left[1 + \left(\frac{E_e}{E_b} \right)^s \right]^{\frac{\alpha_1 - \alpha_2}{s}} \exp \left[- \left(\frac{E_e}{E_{e,\text{cut}}} \right)^\beta \right], \quad (5)$$

where E_e is the lepton energy, E_b the break energy, $E_{e,\text{cut}}$ the cutoff energy, s the smooth parameter, and β the cut-off shape parameter. Based on the results in Zhang et al. (2020), $s = 1$ and $\beta = 3$ are adopted. α_1 and α_2 are the PL index below and above the break energy, respectively. A_e is the normalization parameter and is derived from the total energy in leptons with energy above 1 GeV, W_e .

Besides the cosmic microwave background, the infrared (IR) seed photons are also included for the IC process, which depend on the position in the Galaxy. According to the approximate calculation method presented in Shibata et al. (2011), the energy density of the IR component varies from 0.4 to the maximum value ~ 0.8 eV cm^{-3} when the distance increases from 1 kpc

⁴ <https://www.atnf.csiro.au/research/pulsar/psrcat/>

to ~ 7 kpc toward the direction of the LHAASO source. For the energy density of the IR photon field, the median value of 0.6 eV cm^{-3} with a temperature of 35 K, corresponding to a distance of 3.4 kpc, is adopted. Because there are only H.E.S.S. and LHAASO data, the model parameters are strongly degenerated and cannot be well constrained, especially for α_1 and E_b . For these two parameters, we take some typical values $\alpha_1 = 1.4$ and $E_b = [0.1, 1.0, 10] \text{ TeV}$. Combining the radio and X-ray flux upper limits (see Section 3.4), the fitted SEDs are displayed in Figure 8, and the corresponding parameters are listed in Table 6.

To avoid exceeding the X-ray upper limits, the average magnetic field should be less than $3 \mu\text{G}$. At the same time, α_2 and $E_{e,\text{cut}}$ are acceptable according to the known γ -ray-bright mature PWNe ($t_{\text{psr}} > \sim 10 \text{ kyr}$, where t_{psr} is the PSR age, Zhu et al. 2018). The order of magnitude of the total energy in the evolved electrons at the current stage is 10^{47} erg . Considering the radiative loss, the escape process, etc, the spin-down luminosity of the putative PSR should satisfy $L_{\text{sd}} > 3 \times 10^{35} (t_{\text{psr}}/10 \text{ kyr})^{-1} (d/3.4 \text{ kpc})^{-2} \text{ erg s}^{-1}$. With this condition, there are about 100 PSRs in the ATNF catalogue if the characteristic age is limited in the range from 10^4 to 10^5 yr . So it is very possible that PSRs with the above properties are not detected but power detectable PWNe in the γ -ray band. Based on the current data, therefore, we cannot rule out the scenario in which an evolved PWN powered by a putative PSR produces the measured γ -rays.

5. CONCLUSION

We study the TeV γ -ray emission around SNR-HIIR complex G35.6–0.4 using 796 days of LHAASO-WCDA data and 1216 days of LHAASO-KM2A data. After subtracting the possible contamination from other sources, 1LHAASO J1857+0203u is detected and fitted by an extended 2D-Gaussian source template with an extension of $r_{39} \sim 0.18^\circ$ in the energy range of 1–25 TeV (WCDA component), and a point-like source template at energies above 25 TeV (KM2A component), respectively. The PL spectral indexes of the WCDA and KM2A components are ~ 2.46 and ~ 3.22 , respectively. The statistical significance of the γ -ray signal reaches 11.6σ above 100 TeV.

We investigated three possibilities to explain the detected γ -ray emission. In the scenario that HIIR G35.6–0.5 is a likely source of the high-energy photons, the γ -ray emission can be fitted by a PL spectrum with an exponential cutoff with a proton index of ~ 2.0 and a cutoff energy of $\sim 450 \text{ TeV}$. Despite the absence of massive stars (OB stars), this scenario cannot be completely ruled out. Future multi-wavelength ob-

servations are expected to discover massive stars in the HIIR. If this is the case, G35.6–0.5 is possibly the first HII region with detected γ -ray emission up to 100 TeV energies. In the SNR scenario, due to the low masses of the molecular clouds, it seems unlikely that the TeV γ -rays arise from the clouds illuminated by the protons that escaped from SNR G35.6–0.4. In the scenario that an evolved PWN is powered by a putative PSR, the spin-down luminosity of the PSR should satisfy $L_{\text{sd}} > 3 \times 10^{35} (t_{\text{psr}}/10 \text{ kyr})^{-1} (d/3.4 \text{ kpc})^{-2} \text{ erg s}^{-1}$. The search for PSRs near the centre of the TeV γ -ray emissions would be helpful to explore this possibility. Additionally, with better angular resolution, LACT (Zhang 2023), ASTRI (D’Ai et al. 2022), and CTA (Cherenkov Telescope Array Consortium et al. 2019) may provide clues as to whether the GeV and TeV γ -ray sources are separate sources of different origins.

ACKNOWLEDGEMENTS

This publication makes use of data from FUGIN, FOREST Unbiased Galactic plane Imaging survey with the Nobeyama 45-m telescope, a legacy project in the Nobeyama 45-m radio telescope. This work makes use of Very Large Array Galactic Plane Survey (VGPS) data. The VGPS is supported by a grant from the Natural Sciences and Engineering Research Council of Canada and from the U.S. National Science Foundation. The National Radio Astronomy Observatory is a facility of the National Science Foundation operated under cooperative agreement by Associated Universities, Inc. This work has made use of data from the European Space Agency (ESA) mission *Gaia* (<https://www.cosmos.esa.int/gaia>), processed by the *Gaia* Data Processing and Analysis Consortium (DPAC, <https://www.cosmos.esa.int/web/gaia/dpac/consortium>). Funding for the DPAC has been provided by national institutions, in particular the institutions participating in the *Gaia* Multilateral Agreement. This work is supported in China by NSFC grants under nos. 12393852, 12173018, 12121003, and U1931204 and the National Key R&D program of China under grants 2018YFA0404201, 2018YFA0404202, 2018YFA0404203, and 2018YFA0404204, and in Thailand by the National Science and Technology Development Agency (NSTDA) and the National Research Council of Thailand (NRCT) under the High-Potential Research Team Grant Program (N42A650868). W.J.Z. and X.Z. thank Silvia Celli for helpful discussions. The authors would like to thank all staff members who work at the LHAASO site 4410 m above sea level year-round to maintain the detector and keep the electrical power supply and other components of the experiment operating smoothly. We are grateful

to the Chengdu Management Committee of Tianfu New Area for their constant financial support of research with LHAASO data.

AUTHOR CONTRIBUTIONS

Y.C. initiated and organised this study; W.J.Z. performed the data analyses of the LHAASO (WCDA+KM2A), CO-line, HI, and radio observations, and analysed the optical survey data under the guidance of B.Q.C.; X.Z. and Y.C. led the theoretical interpretation; W.J.Z., X.Z., and Y.C. prepared the manuscript. S.Q.X. and S.Z.C. provided the pipeline for the KM2A

data analysis. S.C.H. and M.Z. provided the pipeline for the WCDA data analysis. H.R.W. provided the cross-check. All other authors participated in data analysis, including detector calibration, data processing, event reconstruction, data quality check, and various simulations, and provided comments on the manuscript.

Software: APLpy (Robitaille & Bressert 2012; Robitaille 2019), Astropy (Astropy Collaboration et al. 2013, 2018), Naima (Zabalza 2015)

REFERENCES

- Abdollahi, S., Acero, F., Baldini, L., et al. 2022, *ApJS*, 260, 53, doi: [10.3847/1538-4365/ac6751](https://doi.org/10.3847/1538-4365/ac6751)
- Abeysekara, A. U., Albert, A., Alfaro, R., et al. 2017, *The Astrophysical Journal*, 843, 39, doi: [10.3847/1538-4357/aa7555](https://doi.org/10.3847/1538-4357/aa7555)
- Abeysekara, A. U., Albert, A., Alfaro, R., et al. 2017, *Science*, 358, 911, doi: [10.1126/science.aan4880](https://doi.org/10.1126/science.aan4880)
- . 2020, *PhRvL*, 124, 021102, doi: [10.1103/PhysRevLett.124.021102](https://doi.org/10.1103/PhysRevLett.124.021102)
- . 2021, *Nature Astronomy*, 5, 465, doi: [10.1038/s41550-021-01318-y](https://doi.org/10.1038/s41550-021-01318-y)
- Adams, C. B., Benbow, W., Brill, A., et al. 2021, *ApJ*, 913, 115, doi: [10.3847/1538-4357/abf926](https://doi.org/10.3847/1538-4357/abf926)
- Aharonian, F., Yang, R., & de Oña Wilhelmi, E. 2019, *Nature Astronomy*, 3, 561, doi: [10.1038/s41550-019-0724-0](https://doi.org/10.1038/s41550-019-0724-0)
- Aharonian, F., Akhperjanian, A. G., Barres de Almeida, U., et al. 2008, *A&A*, 477, 353, doi: [10.1051/0004-6361:20078516](https://doi.org/10.1051/0004-6361:20078516)
- Aharonian, F., An, Q., Axikegu, et al. 2021a, *Chinese Physics C*, 45, 025002, doi: [10.1088/1674-1137/abd01b](https://doi.org/10.1088/1674-1137/abd01b)
- . 2021b, *Chinese Physics C*, 45, 085002, doi: [10.1088/1674-1137/ac041b](https://doi.org/10.1088/1674-1137/ac041b)
- Aharonian, F. A., & Atoyan, A. M. 1996, *A&A*, 309, 917
- Akaike, H. 1974, *IEEE Transactions on Automatic Control*, 19, 716
- Albert, A., Alfaro, R., Alvarez, C., et al. 2020, *ApJL*, 896, L29, doi: [10.3847/2041-8213/ab96cc](https://doi.org/10.3847/2041-8213/ab96cc)
- Astropy Collaboration, Robitaille, T. P., Tollerud, E. J., et al. 2013, *A&A*, 558, A33, doi: [10.1051/0004-6361/201322068](https://doi.org/10.1051/0004-6361/201322068)
- Astropy Collaboration, Price-Whelan, A. M., Sipőcz, B. M., et al. 2018, *AJ*, 156, 123, doi: [10.3847/1538-3881/aabc4f](https://doi.org/10.3847/1538-3881/aabc4f)
- Atoyan, A. M., Aharonian, F. A., & Völk, H. J. 1995, *PhRvD*, 52, 3265, doi: [10.1103/PhysRevD.52.3265](https://doi.org/10.1103/PhysRevD.52.3265)
- Baade, W., & Zwicky, F. 1934, *Proceedings of the National Academy of Science*, 20, 259, doi: [10.1073/pnas.20.5.259](https://doi.org/10.1073/pnas.20.5.259)
- Ballet, J., Bruel, P., Burnett, T. H., Lott, B., & The Fermi-LAT collaboration. 2023, arXiv e-prints, arXiv:2307.12546, doi: [10.48550/arXiv.2307.12546](https://doi.org/10.48550/arXiv.2307.12546)
- Berezinskii, V. S., Bulanov, S. V., Dogiel, V. A., & Ptuskin, V. S. 1990, *Astrophysics of Cosmic Rays* (Amsterdam: North-Holland)
- Beuther, H., Bühr, S., Rugel, M., et al. 2016, *A&A*, 595, A32, doi: [10.1051/0004-6361/201629143](https://doi.org/10.1051/0004-6361/201629143)
- Cao, Z., Aharonian, F. A., An, Q., et al. 2021, *Nature*, 594, 33, doi: [10.1038/s41586-021-03498-z](https://doi.org/10.1038/s41586-021-03498-z)
- Cao, Z., Aharonian, F., An, Q., et al. 2024, *ApJS*, 271, 25, doi: [10.3847/1538-4365/acfd29](https://doi.org/10.3847/1538-4365/acfd29)
- Chen, B. Q., Huang, Y., Hou, L. G., et al. 2019, *MNRAS*, 487, 1400, doi: [10.1093/mnras/stz1357](https://doi.org/10.1093/mnras/stz1357)
- Chen, Y., Bi, X.-J., Fang, K., et al. 2022, *Chinese Physics C*, 46, 030002, doi: [10.1088/1674-1137/ac3fa8](https://doi.org/10.1088/1674-1137/ac3fa8)
- Cherenkov Telescope Array Consortium, Acharya, B. S., Agudo, I., et al. 2019, *Science with the Cherenkov Telescope Array*, doi: [10.1142/10986](https://doi.org/10.1142/10986)
- Cui, Y., Xin, Y., Liu, S., et al. 2021, *A&A*, 646, A114, doi: [10.1051/0004-6361/202039041](https://doi.org/10.1051/0004-6361/202039041)
- D’Ài, A., Amato, E., Burtovoi, A., et al. 2022, *Journal of High Energy Astrophysics*, 35, 139, doi: [10.1016/j.jheap.2022.06.006](https://doi.org/10.1016/j.jheap.2022.06.006)
- de Jager, O. C., Ferreira, S. E. S., Djannati-Ataï, A., et al. 2009, arXiv e-prints, arXiv:0906.2644, doi: [10.48550/arXiv.0906.2644](https://doi.org/10.48550/arXiv.0906.2644)
- Fleysher, R., Fleysher, L., Nemethy, P., Mincer, A. I., & Haines, T. J. 2004, *ApJ*, 603, 355, doi: [10.1086/381384](https://doi.org/10.1086/381384)
- Frerking, M. A., Langer, W. D., & Wilson, R. W. 1982, *ApJ*, 262, 590, doi: [10.1086/160451](https://doi.org/10.1086/160451)
- Fujita, Y., Ohira, Y., & Takahara, F. 2010, *ApJL*, 712, L153, doi: [10.1088/2041-8205/712/2/L153](https://doi.org/10.1088/2041-8205/712/2/L153)

- Gabici, S., Aharonian, F. A., & Casanova, S. 2009, *MNRAS*, 396, 1629, doi: [10.1111/j.1365-2966.2009.14832.x](https://doi.org/10.1111/j.1365-2966.2009.14832.x)
- Gaia Collaboration, Prusti, T., de Bruijne, J. H. J., et al. 2016, *A&A*, 595, A1, doi: [10.1051/0004-6361/201629272](https://doi.org/10.1051/0004-6361/201629272)
- Gaia Collaboration, Vallenari, A., Brown, A. G. A., et al. 2023a, *A&A*, 674, A1, doi: [10.1051/0004-6361/202243940](https://doi.org/10.1051/0004-6361/202243940)
- Gaia Collaboration, Creevey, O. L., Sarro, L. M., et al. 2023b, *A&A*, 674, A39, doi: [10.1051/0004-6361/202243800](https://doi.org/10.1051/0004-6361/202243800)
- Ginzburg, V. L., & Syrovatskii, S. I. 1964, *The Origin of Cosmic Rays*
- Gould, R. J., & Schröder, G. P. 1967, *Physical Review*, 155, 1404, doi: [10.1103/PhysRev.155.1404](https://doi.org/10.1103/PhysRev.155.1404)
- H. E. S. S. Collaboration, Abdalla, H., Abramowski, A., et al. 2018, *A&A*, 612, A1, doi: [10.1051/0004-6361/201732098](https://doi.org/10.1051/0004-6361/201732098)
- HESS Collaboration, Abramowski, A., Aharonian, F., et al. 2016, *Nature*, 531, 476, doi: [10.1038/nature17147](https://doi.org/10.1038/nature17147)
- Kafexhiu, E., Aharonian, F., Taylor, A. M., & Vila, G. S. 2014, *PhRvD*, 90, 123014, doi: [10.1103/PhysRevD.90.123014](https://doi.org/10.1103/PhysRevD.90.123014)
- Lande, J., Ackermann, M., Allafort, A., et al. 2012, *ApJ*, 756, 5, doi: [10.1088/0004-637X/756/1/5](https://doi.org/10.1088/0004-637X/756/1/5)
- Li, H., & Chen, Y. 2012, *MNRAS*, 421, 935, doi: [10.1111/j.1365-2966.2012.20270.x](https://doi.org/10.1111/j.1365-2966.2012.20270.x)
- Liu, Y.-M., Zeng, H.-D., Xin, Y.-L., Liu, S.-M., & Zhang, Y. 2024, *Research in Astronomy and Astrophysics*, 24, 075016, doi: [10.1088/1674-4527/ad50b7](https://doi.org/10.1088/1674-4527/ad50b7)
- Ma, X.-H., Bi, Y.-J., Cao, Z., et al. 2022, *Chinese Physics C*, 46, 030001, doi: [10.1088/1674-1137/ac3fa6](https://doi.org/10.1088/1674-1137/ac3fa6)
- MAGIC Collaboration, Aleksić, J., Ansoldi, S., et al. 2014, *A&A*, 571, A96, doi: [10.1051/0004-6361/201423517](https://doi.org/10.1051/0004-6361/201423517)
- MAGIC Collaboration, Acciari, V. A., Ansoldi, S., et al. 2020, *A&A*, 642, A190, doi: [10.1051/0004-6361/201936896](https://doi.org/10.1051/0004-6361/201936896)
- Malone, K., Andrés García González, J., & Harding, P. 2023, *arXiv e-prints*, arXiv:2311.00861, doi: [10.48550/arXiv.2311.00861](https://doi.org/10.48550/arXiv.2311.00861)
- Manchester, R. N., Hobbs, G. B., Teoh, A., & Hobbs, M. 2005, *AJ*, 129, 1993, doi: [10.1086/428488](https://doi.org/10.1086/428488)
- Nagahama, T., Mizuno, A., Ogawa, H., & Fukui, Y. 1998, *AJ*, 116, 336, doi: [10.1086/300392](https://doi.org/10.1086/300392)
- Ohira, Y., Murase, K., & Yamazaki, R. 2011, *MNRAS*, 410, 1577, doi: [10.1111/j.1365-2966.2010.17539.x](https://doi.org/10.1111/j.1365-2966.2010.17539.x)
- Paredes, J. M., Ishwara-Chandra, C. H., Bosch-Ramon, V., et al. 2014, *A&A*, 561, A56, doi: [10.1051/0004-6361/201322306](https://doi.org/10.1051/0004-6361/201322306)
- Paron, S., & Giacani, E. 2010, *A&A*, 509, L4, doi: [10.1051/0004-6361/200913694](https://doi.org/10.1051/0004-6361/200913694)
- Paron, S., Giacani, E., Rubio, M., & Dubner, G. 2011, *A&A*, 530, A25, doi: [10.1051/0004-6361/201016390](https://doi.org/10.1051/0004-6361/201016390)
- Planck Collaboration, Abergel, A., Ade, P. A. R., et al. 2014, *A&A*, 571, A11, doi: [10.1051/0004-6361/201323195](https://doi.org/10.1051/0004-6361/201323195)
- Planck Collaboration, Aghanim, N., Ashdown, M., et al. 2016, *A&A*, 596, A109, doi: [10.1051/0004-6361/201629022](https://doi.org/10.1051/0004-6361/201629022)
- Portegies Zwart, S. F., McMillan, S. L. W., & Gieles, M. 2010, *ARA&A*, 48, 431, doi: [10.1146/annurev-astro-081309-130834](https://doi.org/10.1146/annurev-astro-081309-130834)
- Reich, W., Fuerst, E., Haslam, C. G. T., Steffen, P., & Reif, K. 1984, *A&AS*, 58, 197
- Reid, M. J., Menten, K. M., Brunthaler, A., et al. 2014, *ApJ*, 783, 130, doi: [10.1088/0004-637X/783/2/130](https://doi.org/10.1088/0004-637X/783/2/130)
- Robitaille, T. 2019, *APLpy v2.0: The Astronomical Plotting Library in Python, 2.0*, Zenodo, Zenodo, doi: [10.5281/zenodo.2567476](https://doi.org/10.5281/zenodo.2567476)
- Robitaille, T., & Bressert, E. 2012, *APLpy: Astronomical Plotting Library in Python*, *Astrophysics Source Code Library*, record ascl:1208.017. <http://ascl.net/1208.017>
- Rohlfs, K., & Wilson, T. L. 2004, *Tools of radio astronomy*
- Salpeter, E. E. 1955, *ApJ*, 121, 161, doi: [10.1086/145971](https://doi.org/10.1086/145971)
- Shibata, T., Ishikawa, T., & Sekiguchi, S. 2011, *ApJ*, 727, 38, doi: [10.1088/0004-637X/727/1/38](https://doi.org/10.1088/0004-637X/727/1/38)
- Stil, J. M., Taylor, A. R., Dickey, J. M., et al. 2006, *AJ*, 132, 1158, doi: [10.1086/505940](https://doi.org/10.1086/505940)
- Tibolla, O. 2023, in *Journal of Physics Conference Series*, Vol. 2429, *Journal of Physics Conference Series (IOP)*, 012017, doi: [10.1088/1742-6596/2429/1/012017](https://doi.org/10.1088/1742-6596/2429/1/012017)
- Umamoto, T., Minamidani, T., Kuno, N., et al. 2017, *PASJ*, 69, 78, doi: [10.1093/pasj/psx061](https://doi.org/10.1093/pasj/psx061)
- Wang, Y., Beuther, H., Rugel, M. R., et al. 2020, *A&A*, 634, A83, doi: [10.1051/0004-6361/201937095](https://doi.org/10.1051/0004-6361/201937095)
- Wenger, M., Ochsenbein, F., Egret, D., et al. 2000, *A&AS*, 143, 9, doi: [10.1051/aas:2000332](https://doi.org/10.1051/aas:2000332)
- Wenger, T. V., Balsler, D. S., Anderson, L. D., & Bania, T. M. 2018, *ApJ*, 856, 52, doi: [10.3847/1538-4357/aaec8](https://doi.org/10.3847/1538-4357/aaec8)
- Wilks, S. S. 1938, *The Annals of Mathematical Statistics*, 9, 60, doi: [10.1214/aoms/1177732360](https://doi.org/10.1214/aoms/1177732360)
- Zabalza, V. 2015, in *International Cosmic Ray Conference*, Vol. 34, *34th International Cosmic Ray Conference (ICRC2015)*, 922, doi: [10.22323/1.236.0922](https://doi.org/10.22323/1.236.0922)
- Zhang, S. 2023, *PoS, ICRC2023*, 808, doi: [10.22323/1.444.0808](https://doi.org/10.22323/1.444.0808)
- Zhang, X., Chen, Y., Huang, J., & Chen, D. 2020, *MNRAS*, 497, 3477, doi: [10.1093/mnras/staa2151](https://doi.org/10.1093/mnras/staa2151)
- Zhang, X., Chen, Y., Zheng, F.-x., et al. 2022, *ApJ*, 931, 128, doi: [10.3847/1538-4357/ac6957](https://doi.org/10.3847/1538-4357/ac6957)
- Zhu, B.-T., Zhang, L., & Fang, J. 2018, *A&A*, 609, A110, doi: [10.1051/0004-6361/201629108](https://doi.org/10.1051/0004-6361/201629108)

Zhu, H., Tian, W. W., Torres, D. F., Pedalletti, G., & Su,
H. Q. 2013, *ApJ*, 775, 95,
doi: [10.1088/0004-637X/775/2/95](https://doi.org/10.1088/0004-637X/775/2/95)

APPENDIX

A. GAMMA-RAY ABSORPTION

To calculate the $\gamma - \gamma$ absorption, we use the pair production cross section in [Gould & Schröder \(1967\)](#) and the interstellar radiation field in [Shibata et al. \(2011\)](#). The results are displayed in Figure 9, showing the limited impact on the flux for $d = 3.4$ kpc. Thus we only consider the $\gamma - \gamma$ absorption in the SNR scenario in which the distance $d = 10.5$ kpc is adopted.

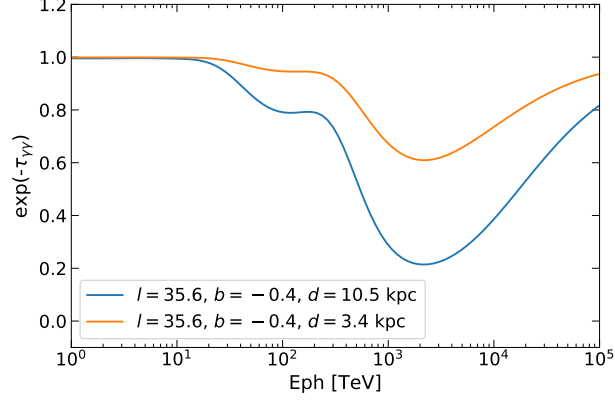


Figure 9. The survive probability due to the $\gamma - \gamma$ absorption.

B. SNR SCENARIO

To explain the LHAASO data, the mass of clouds should be larger than the measured values. In Figure 10, as an example, the mass of Cloud K is amplified by a factor of f_K . The corresponding fitted parameters can be found in Table 7.

Table 7. Parameters for the SNR scenario.

| η | α | δ | χ | s | $E_{p,\max}$ (PeV) | f_K^a |
|--------|----------|----------|--------|-------|--------------------|---------|
| 0.1 | 2.0 | 0.3 | 0.05 | 2.553 | 0.6 | 3.0 |
| 0.1 | 2.0 | 0.5 | 0.01 | 2.685 | 1.0 | 4.0 |
| 0.1 | 2.0 | 0.7 | 0.0015 | 2.968 | 3.0 | 5.0 |

Notes.

^a The mass of Cloud K is amplified by a factor of f_K .

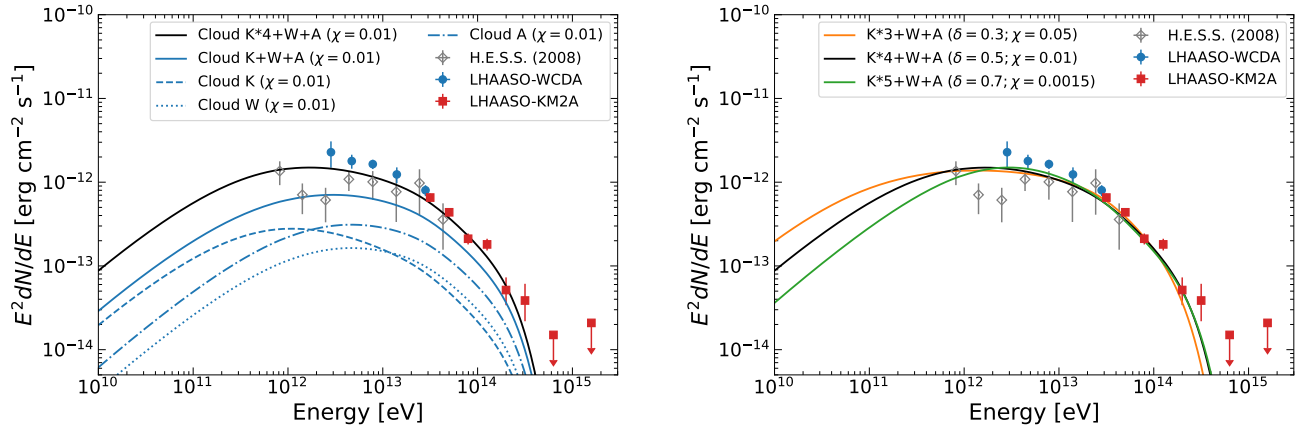


Figure 10. Fitted SED of the SNR scenario including the $\gamma-\gamma$ absorption. *Left:* The blue solid line represents the total γ -ray emission from Cloud K, W, and A with $\delta = 0.5$ and $\chi = 0.01$. For the black solid line, the component of Cloud K is amplified by a factor of 4. *Right:* The γ -ray emission produced by the escaped protons is displayed in red, black, and green solid lines for $\delta = 0.3, 0.5$, and 0.7 , respectively. The detailed parameters can be found in Table 7.